

THESIS

THE ROLE OF MOISTURE IN THE MJO: A COMPARISON OF TROPICAL
CONVECTION PROCESSES IN THE CAM AND SUPER-PARAMETERIZED CAM

Submitted By:

Katherine Thayer-Calder

Department of Atmospheric Science

In partial fulfillment of the requirements

For the Degree of Master of Science

Colorado State University

Fort Collins, Colorado

Spring 2008

COLORADO STATE UNIVERSITY

January 29, 2008

WE HEREBY RECOMMEND THAT THE THESIS PREPARED UNDER OUR SUPERVISION BY KATHERINE THAYER-CALDER ENTITLED THE ROLE OF MOISTURE IN THE MJO: A COMPARISON OF TROPICAL CONVECTION PROCESSES IN THE CAM AND SUPER-PARAMETERIZED CAM BE ACCEPTED AS FULFILLING IN PART REQUIREMENTS FOR THE DEGREE OF MASTER OF SCIENCE.

Committee on Graduate Work

Advisor

Department Head

ABSTRACT OF THESIS

THE ROLE OF MOISTURE IN THE MJO: A COMPARISON OF TROPICAL CONVECTION PROCESSES IN THE CAM AND SUPER-PARAMETERIZED CAM

Despite nearly 40 years of research on the phenomenon, questions still surround many of the fundamental aspects of the Madden-Julian Oscillation (MJO). Many observational studies have been able to describe the physical structure of this very large region of convection that reappears every 30 to 60 days in the Indian Ocean and slowly travels eastward into the Western Pacific. However, the source of the disturbance, the processes controlling the evolution of the convection, and the feedbacks required to create and maintain the MJO are not well understood.

This study compares data from two models which differ primarily in their convection parameterizations but produce extremely different MJO signals. The Community Atmosphere Model (CAM) version 3.0 from NCAR uses the Zhang and McFarlane (1995) scheme as well as the Hack (1994) shallow convection parameterization and does not produce an MJO. The Super Parameterized version of the CAM (SP-CAM) replaces these convection parameterizations with a two dimensional cloud resolving model (CRM) in each gridcell (Khairoutdinov and Randall 2001) and produces an extremely vigorous MJO. Data from the ERA-40 reanalysis and TOGA-COARE observational study are also presented.

Our analysis supports the Discharge Recharge Oscillation (DRO) theory proposed by Bladé and Hartmann (1993), which stipulates that the appearance of the MJO is based on the time period required to moisten and destabilize the troposphere above the Indian Ocean

and western Pacific. The CAM is unable to produce a moistened atmosphere through many levels because of unrealistic constraints placed on its convection parameterizations. Without a nearly saturated column, convection that appears soon dies out due to local negative feedbacks. The SP-CAM produces an overly moist column due to unrealistic winds and evaporation during strong convective events. In the real tropics and the SP-CAM, the convection within a high humidity environment produces more intense heating and spawns the large scale circulation that is the signature of the MJO. The analyses show that the processes that produce water vapor through the entire tropical troposphere must be accurately represented in a model in order to generate the environment necessary for an MJO.

Katherine Thayer-Calder
Department of Atmospheric Science
Colorado State University
Fort Collins, CO 80523

Spring 2008

Acknowledgments

I would like to extend profound thanks to my advisor Dr. David A. Randall, without whom this thesis would not exist. I have learned more from him in the last few years than I ever expected or imagined. It has been an honor to work with him. I would also like to thank my thesis committee members, Dr. Graeme Stephens and Dr. Adele Howe, for their guidance and helpful suggestions.

Roger Marchand, Steven Ghan, Nathaniel Beagley, Thomas Ackerman and several other scientists at Pacific Northwest National Laboratories have provided invaluable help to the completion of this project, including the data upon which most of the analysis is based.

A huge thank-you goes out to everybody in the Randall research group. So many of them have contributed to this thesis in so many ways. Special thanks to Jim Benedict who has been an enormous source of help throughout this process.

My husband, Mark, deserves a special debt of gratitude. His steadfast support and amazingly selfless sacrifice throughout this process has been superhuman.

This work was funded by a National Science Foundation (NSF) grant ATM-0415184. This research was partially supported by the Office of Science (BER), U.S. Department of Energy, Cooperative Agreement No. DE-FC02-01ER63163. This work was also supported in part by the National Science and Technology Center for Multi-Scale Modeling of Atmospheric Processes, managed by Colorado State University under Cooperative Agreement ATM-0425247.

Table of Contents

SIGNATURE PAGE	ii
ABSTRACT OF THESIS	iii
ACKNOWLEDGEMENTS	v
TABLE OF CONTENTS	vi
LIST OF TABLES	vii
LIST OF FIGURES	viii
Chapter 1: Introduction	1
A. Background and Motivation	1
B. Overview of MJO Observations	6
C. The Discharge-Recharge Oscillation	9
Chapter 2: Models, Data and Methods	13
A. About the Models	13
B. Observational Data	24
C. Methodology	26
Chapter 3: Results, Analysis and Discussion	32
A. Large-Scale Properties of the MFR	32
B. Convective Moistening and Drying	41
C. The Discharge-Recharge Oscillation	49
D. Convective Heating and Large-Scale Circulations	53
Chapter 4: Summary and Future Work	61
REFERENCES	69

List of Tables

TABLE 1: Overview of parameterization assumptions and simplifications, reasoning behind each in blue	23
TABLE 2: Overview of the data used in this analysis	25

List of Figures

FIG 1: A map showing the impacts and teleconnections of MJO	2
FIG 2: Wavenumber-period power spectrum normalized by the background spectrum for the OLR in the SP-CAM (first), CAM (second) and ECMWF ERA-40 reanalysis (third)	5
FIG 3: A series of longitude-height diagrams illustrating the major steps during the life of a typical MJO (from Madden and Julian, 1972)	7
FIG 4: The MJO convective envelope is made up of many smaller storms. Figure from Nakazawa (1988)	8
FIG 5: A schematic of the basic vertical structure of the convective center of the MJO (from Rui and Wang 1990)	9
FIG 6: Illustration of the Discharge-Recharge oscillation described by Bladé and Hartmann (1993) that shows the asymmetry in the MJO	10
FIG 7: A brief illustration of the cloud model in the Zhang and MacFarlane (1995) deep convection parameterization	14
FIG 8: A brief illustration of the cloud model in the Hack (1994) convection parameterization	17
FIG 9: An illustration of the stratiform cloud parameterization in the CAM	19
FIG 10: A simple illustration of the architecture of the Super Parameterization in the CAM	21
FIG 11: A map of the Equatorial Focus Region (EFR) and the MJO Focus Region (MFR)	26
FIG 12: Time-longitude plots of OLR (color contours) along the equator, MJO filtered values (thin lines) and selected MJO events (thick lines)	28

FIG 13: Maps showing the location of the points determined to be lowest value of filtered OLR in selected MJO events	29
FIG 14: A map of the TOGA-COARE priority sounding sites	30
FIG 15: Map of mean zonal winds at 850 hPa between 16S and 16N around the globe for the SP-CAM (top), CAM (middle) and ERA-40 (bottom) during the entire four year period analyzed	33
FIG 16: Histograms of gridcells with a given daily average rainrate for the four years of data used in this study	34
FIG 17: Average vertical velocity profiles for each value of daily average rainrate in the MFR of the SP-CAM, the CAM, ERA-40 with ERA-40 rainrates and ERA-40 with TRMM rainrates	35
FIG 18: Averaged static stability profiles for each value of daily average rainrate in the MFR of the SP-CAM (top), CAM (middle) and ERA-40 reanalysis with TRMM precipitation (bottom)	37
FIG 19: Averaged potential temperature profiles for each value of daily averaged rainrate in the MR of the SP-CAM (top), the CAM (middle) and ERA-40 with TRMM precipitation (bottom)	38
FIG 20: Averaged ARC profiles for each value of daily average rainrate in the MFR of the SP-CAM (top) and the CAM (bottom)	39
FIG 21: Average moist static energy profiles for each value of daily averaged rainrae in the MFR of the SP-CAM (top), the CAM (middle), and ERA-40 with TRMM precipitation (bottom)	40
FIG 22: Average value of Total Precipitable Water (TPW) or total column water vapor for each value of daily average rainrate in the MFR	42

FIG 23: Percentage of daily average rainrate attributed o each of the three precipitating parameterizations in the CAM per value of daily average rainrate in the MFR of the SP-CAM (top) and the CAM (bottom)	42
FIG 24: Composite profiles of relative humidity for each value of rainrate in the MFR of the SP-CAM (top), the CAM (second), ERA-40 reanalysis with TRMM rainrates (third), and TOGA-COARE data (bottom)	43
FIG 25: Change in TPW between three hourly averages composited by the corresponding six hour running mean of precipitation	45
FIG 26: Composite profiles of the components of the local moisture budget (evaporation, precipitation and change in total column vapor) for the MFR of the SP-CAM (top), the CAM (middle) and ERA-40 reanalysis (bottom)	46
FIG 27: Composite plot of surface wind speed per value of rainrate for the MFR of the SP-CAM, the CAM, the ERA-40 reanalysis, and TOGA-COARE data	47
FIG 28: Composite plots of the vertical profiles of relative humidity with respect to time before and after the passage of an MJO or strong rain event in the SP-CAM (top) and CAM (bottom)	50
FIG 29: The cycle of Discharge and Recharge in the CAM and SP-CAM (top), ERA-40 and TRMM (middle) and TOGA-COARE (bottom)	51
FIG 30: Composite plots of the precipitation, OLR ad TPW during the passage of the MJO or strong rain event in the SP-CAM (top) and the CAM (bottom)	52
FIG 31: Q_1 heating rate (apparent heat source) profiles per value of rainrate in the SP-CAM (top) and the CAM (bottom)	54
FIG 32: Q_2 drying rate (apparent moisture sink) profiles per value of rainrate in the SP-CAM (top) and the CAM (bottom)	55

FIG 33: Profile of Q_1 with the passage of a composite MJO or strong rain event in the SP-CAM (top), CAM (middle) and the IFA-average derived Q_1 smoothed with a 5 day running mean for the first MJO event during TOGA-COARE (bottom) 57

FIG 34: Profile of Q_2 with passage of a composite MJO or strong rain event in the SP-CAM (top), CAM (middle) and the IFA-average derived Q_2 smoothed with a 5 day running mean for the first MJO during TOGA-COARE (bottom) 58

FIG 35: Surface wind speed (vectors) and surface relative humidity (color contours) for an MJO or strong rain event at minimum filtered OLR in the SP-CAM (top) and the CAM (bottom) 59

Chapter 1: Introduction

A. Background and Motivation

The Earth's atmosphere can do amazing things. It produces beautiful clouds, blocks harmful radiation from space, and provides chemical nutrients necessary for almost all life on the planet. The atmosphere works to transport heat from the tropics to the poles in order to efficiently cool the planet, but absorbs and re-radiates heat from the surface to keep terrestrial temperatures warm. The atmosphere helps to sustain life on the planet, but can produce vicious and deadly tornados, typhoons, and violent weather systems that stir up the ocean and decimate the land. And once every 30 to 70 days or so, the atmosphere produces a mass of storms and convection near the equator that is so large and so slow moving that its reverberating effects will be felt around the globe for weeks.

This one to two month oscillation of convection in the tropical Indian and western Pacific oceans is known as an intraseasonal oscillation, or the Madden-Julian Oscillation (MJO). It is considered intraseasonal because the swing from rain, to clear dry skies, and back to rain, takes less than a full season, but more than a couple of weeks. The MJO is a very large, slowly moving, generally equatorial, eastward propagating region of active convection, followed by an equally large and slowly eastward moving region of clear skies and suppressed convection. It spans 50 to 100 degrees of longitude or zonal wavenumbers one to four, and its speed varies generally from four to six m s^{-1} .

The disturbance can be seen in many different atmospheric variables, including upper tropospheric winds, temperature, outgoing longwave radiation (OLR), water vapor and

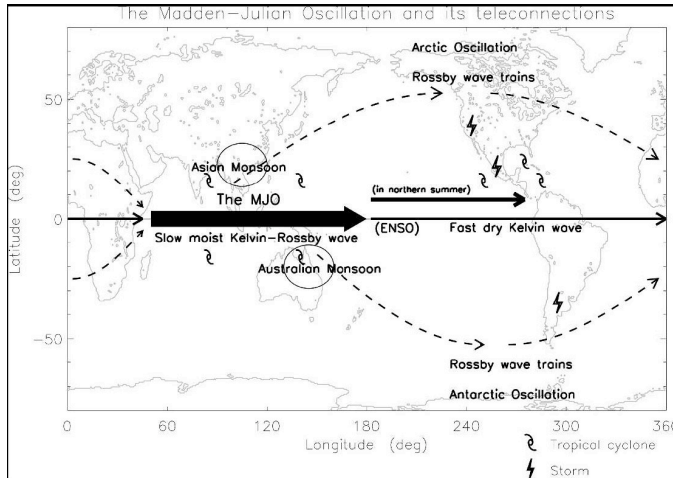


FIG 1: A map showing the impacts and teleconnections of MJO disturbances. The disturbance itself can spawn cyclones in the Indian Ocean, and its effects can modulate the growth of hurricanes in North America and affect precipitation in both North and South America. From Figure 1 in Lin et al. 2006.

precipitation. The convective phase of the MJO usually forms in the eastern or central Indian ocean, and propagates eastward towards Indonesia. Often the MJO dies out near the international date line, and smaller, fast-moving disturbances with less convection, called Kelvin waves, continue to propagate eastward from there (Figure 1). The

MJO system has been shown to affect weather all over the planet, from modulating the growth of tropical storms around the world (Maloney and Hartmann 2000a) to influencing both the Arctic and Antarctic oscillations (Miller et al. 2003). Observational studies of the MJO are reviewed by Madden and Julian (1994) and Zhang (2005). This vast convective disturbance has huge impacts on the weather and climate of our planet, but is actually not well understood. There is no current theory which can explain all aspects of the MJO. Because of the mystery surrounding the phenomenon, it is often poorly formed or completely missing from general circulation model (GCM) simulations (Lin et al. 2006).

GCMs have long been used to further our understanding of the atmosphere (Arakawa et al. 1968) and the global climate system (Manabe et al. 1979). In the past 30 years, models which were once used for research have been streamlined to produce rapid weather forecasts (Gneiting and Raftery 2005), and are now an integral part of short and long-term weather prediction. Increasingly, cutting edge GCM climate forecasts are used to project the myriad possible impacts of climate change (Solomon et al. 2007). They are also used in a wide variety of other applications, such as forecasting the effects of land-use changes (Bonan 1997),

investigating air pollution dispersion patterns (Rasch et al. 2000) and attempting to forecast the effects of nuclear war (Covey et al. 1984). The results of GCMs lend understanding to our chaotic natural world and influence critical economic and political decisions, so it is extremely important that these models be as realistic as possible.

Unfortunately, most GCMs still have major short-comings in their simulations of tropical intraseasonal variability. Slingo et al. (1996 - hereafter S96) provided an early view of the issues many GCMs had in representing the MJO. S96 compared the 200 hPa velocity potential and 200 hPa zonal winds of 15 models from the Atmospheric Model Intercomparison Project (AMIP). While most of the models showed some form of large eastward propagating convective disturbance, generally these moved much faster than the MJO in observations. S96 looked at the power of planetary scale waves at many different speeds, or periods, in each model, and no model showed a realistic spectrum. Most did not have nearly enough power in the range of MJO propagation periods, while showing relatively increased power for faster moving waves. The results also indicated that models without enough intraseasonal variability suffered from too little tropical climatic variability at other scales - such as little seasonal cycle, and low precipitation amounts or unrealistic precipitation distributions throughout the tropics. Thus, the strength of the MJO simulated by a GCM could be a diagnostic of the overall realism of the tropical climate within the model.

A study published by Lin et al. (2006 - hereafter L06) gave a more up-to-date review of the tropical precipitation in 14 GCMs. In this study, each model was coupled to an interactive ocean surface model as well. These 14 models were participants in the Intergovernmental Panel on Climate Change (IPCC) Fourth Assessment Report released in the early months of 2007, and represent the current state-of-the-art in global climate modeling. The study's results show the MJO-related precipitation variance as less than half of the observed variance in 12 of the 14 models. In fact, L06 point out that the MJO variance that does show

up in their analysis of the tropical precipitation power spectrum is often “part of an over-reddened spectrum,” or large power in a spectrum that has too much power for all waves. This is inaccurate because the observed spectrum of tropical precipitation has a pronounced peak at MJO periods, and lower power for other waves. The authors tie this over-reddening to a high persistence of equatorial precipitation, implying that the tropics of these models suffer from constant light rain. L06 suggest that without the variability of heavy rain events and following dry periods, the organization of a large-scale system such as the MJO is impossible. Even after ten years of research and increases in computing power, L06 shows that the capabilities of GCMs to simulate the MJO have not improved much at all.

It is interesting to note that both S96 and L06 point to the details of a model’s statistical representation of convection processes (parameterizations) as being the most important factor in the accuracy of its MJO simulation. However, S96 suggests that models which use a convection parameterization based on convective available potential energy (CAPE) perform better than those based on moisture convergence. L06 found the exact opposite to be true, with the two most realistic models being the only ones using convection parameterizations linked to moisture convergence. This type of confusion and contradictory evidence is prevalent in literature regarding the MJO.

In this study, we compare two models which differ in their convection parameterizations and produce wildly different MJOs. The first is the NCAR Community Atmosphere Model (CAM) version 3.0. This model uses the Zhang and McFarlane (1995) scheme for deep convection, which is a CAPE-based parameterization. The second model is a version of the Super Parameterized CAM (SP-CAM) which is nearly the same as the first model. The main difference between the two is that in each grid cell of the SP-CAM the convection parameterizations have been replaced with a two dimensional Cloud Resolving Model (CRM) (Khairoutdinov and Randall 2001). For more information on the details of the models and

setup for this experiment, see Chapter 2.

Both models were run for the same four-year time period, and both used the same boundary conditions. As discussed in detail later, the CAM produced almost no recognizable MJO disturbances, and has very little power above the background spectrum in the MJO region (see Figure 2). The SP-CAM, however, produced extremely vigorous MJOs, stronger even than the observed disturbances. This presents us with a great opportunity to learn about which convective processes are important for the production and maintenance of a strong and healthy MJO, not just within a model but also in the real atmosphere.

Our goals in this study are three-fold. At the basic level, we hope to better understand the processes missing from the GCMs that are unable to produce an MJO. In order to do this, we will analyze the results of the model simulations using a framework provided by the

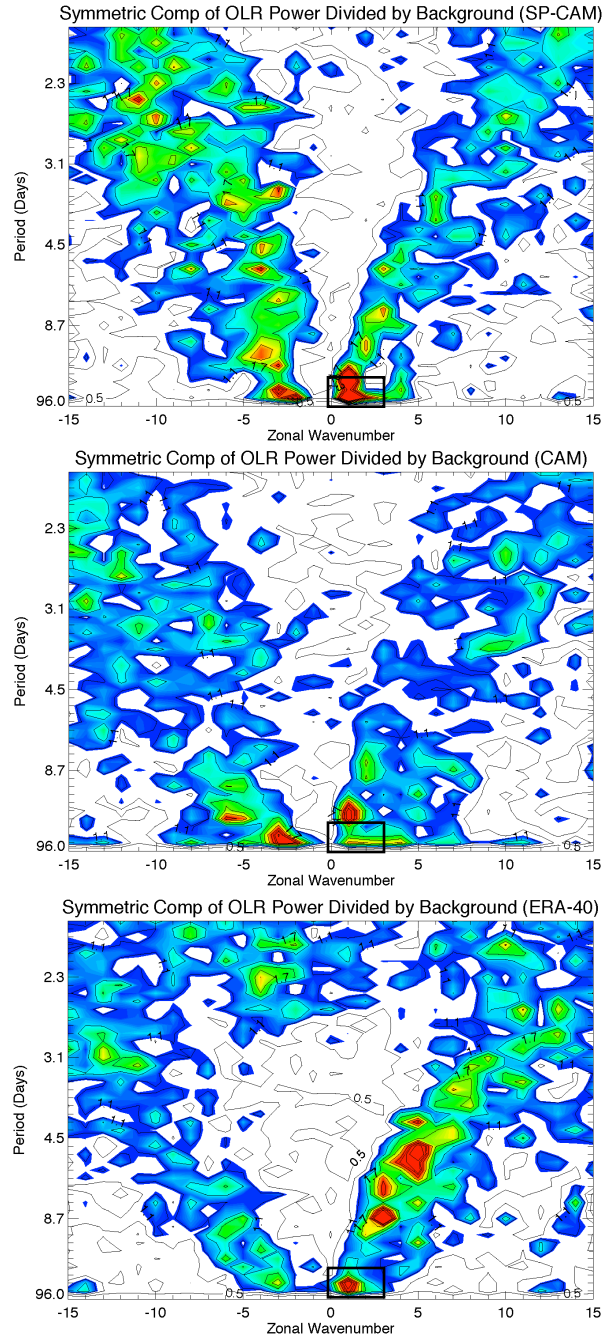


FIG 2: Wavenumber-period power spectrum normalized by the background spectrum for the OLR in the SP-CAM (first), CAM (second) and ECMWF ERA-40 reanalysis (third). See Section II for more information on the formulation of these plots. The region describing the power of the MJO (eastward wavenumbers 1-5 and long periods) is highlighted with black boxes.

Discharge-Recharge oscillation (DRO). This cycle was described by Bladé and Hartmann (1993), and it includes a series of atmospheric processes and feedbacks that are necessary for the organization of convection into large-scale, slowly eastward propagating disturbances. This framework helps us to address the second goal of the study, which is to further examine the validity and importance of the DRO in the creation of the real-world MJO. While still somewhat controversial, the DRO has received support in recent observational and modeling studies (Benedict and Randall 2007, Kemball-Cook and Weare 2001, Wang and Schlesinger 1999, Hu and Randall 1994). Finally and primarily, we hope that the conclusions drawn from this analysis allow us to broaden understanding of the MJO in our physical world.

This study begins with a brief overview of the observed characteristics of the MJO and a description of the Discharge-Recharge oscillation. The second chapter discusses the data sources and plotting methodology, including a detailed discussion of the convection parameterizations of each model. Chapter 3 presents the data analysis. Finally, Chapter 4 presents a summary and proposed future work.

B. Overview of MJO Observations

There have been literally hundreds of papers written on intraseasonal oscillations and tropical convectively-coupled waves since Madden and Julian first described this particular disturbance in their landmark 1971 paper. Despite all of this work, the fundamental mechanisms behind the MJO are still difficult to explain. However, the general physical structure of the disturbance has been well documented, so we can present an overview of the basic observed structure and lifecycle of the MJO in this section.

In 1971, Madden and Julian noticed a spectral peak in their analysis of ten years of 850 hPa and 150 hPa zonal winds at Canton Island in the equatorial West Pacific (Madden and Julian 1971). They were only able to analyze one location, as observational data from the

wide expanses of the tropical oceans was spotty and difficult to come by before the age of observational satellites. Regardless, Madden and Julian's analysis noted a pattern of zonal wind and temperature anomalies appearing much less frequently and more powerfully than the usual synoptic tropical weather disturbances. Their next papers indicated these long-period oscillations traveled eastward, where most shorter-lived and quicker-moving disturbances moved westward with the mean low-level easterly flow (Madden and Julian 1972). They dubbed this eastward propagating wind anomaly the 40-50 Day Oscillation, as that was the location of the pronounced peak in their spectral analysis of data from Canton. The spectral peak (and the name) indicates that the storm-laden disturbance generally appears every 40-50 days at the observation station (Madden and Julian 1971).

Figure 3, at right, is taken from their

1972 paper and describes the general life-cycle of an MJO event. The figures begin with the growth of convection in the Indian ocean, which propagates to the east, with the deepest convection and strongest circulations occurring in the 4th panel, labeled 'A'. In panel 'B', the

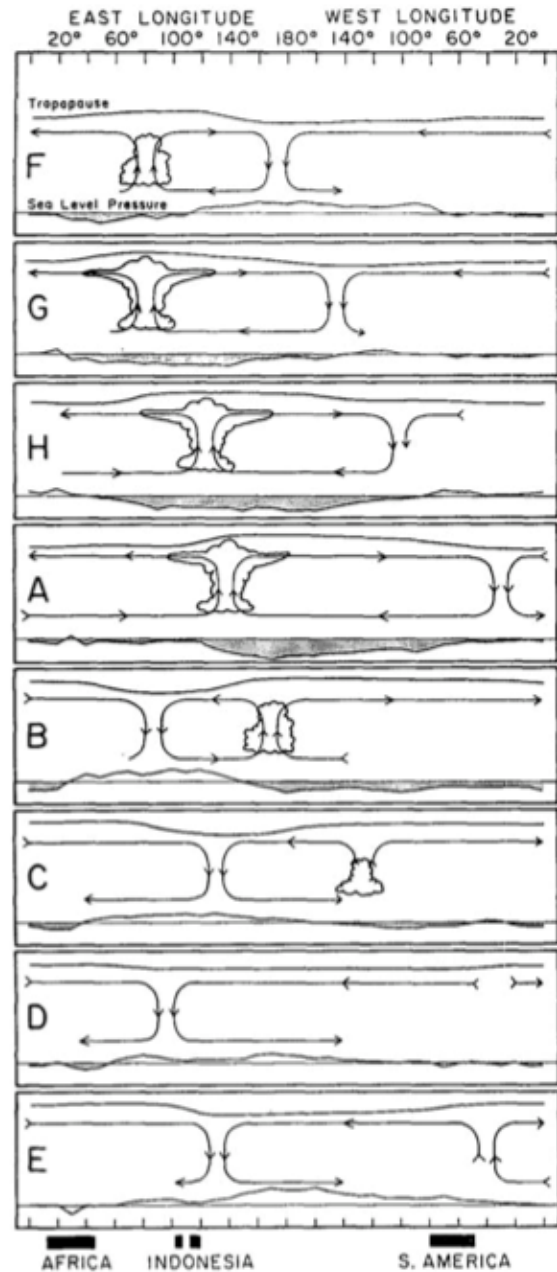


FIG 3: A series of longitude-height diagrams illustrating the major steps during the life of a typical MJO (From Madden and Julian, 1972). Deep convection forms over the Indian Ocean and propagates eastward into the western Pacific Ocean. The zonal wind circulation can continue to propagate from there.

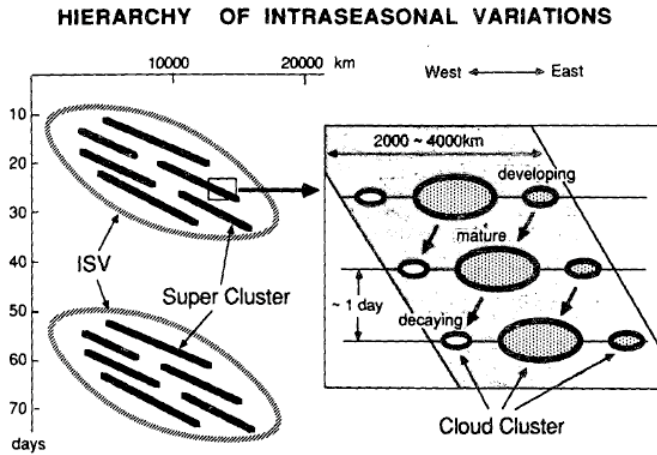


FIG 4: The MJO convective envelope is made up of many smaller storms. Figure from Nakazawa 1988.

convection begins to die out around 180° longitude, and the large-scale circulation of winds continues to propagate from there. Behind the convection is a descending branch of the circulation, which inhibits deep convection in the Indian and Western Pacific oceans for another couple of weeks.

Observations since these early papers have stressed the broadband nature of the periodic reappearance of the disturbance. The time between events can be as little as 20 or as many as 100 days. Also, the disturbances themselves travel on average at four to six m s^{-1} , but the speed varies greatly through their lifetime. While the disturbance is now known as the Madden-Julian Oscillation (MJO), it is not a regular oscillation, and the timescale and frequency of its appearance change season-to-season and year to year (Zhang 2005).

The structure of the convection associated with the MJO is more complicated than what is depicted in Figure 3. Nakazawa (1988), and many studies since, have shown that the large region of convection associated with the MJO is more of a large-scale convective envelope, which contains many smaller storms within it (as in Figure 4). Even though the MJO and its envelope of convection move to the east, storms within the envelope propagate to the west. This multi-scale structure has been examined at length in studies by Lau et al. (1989) and Chen et al. (1996).

As shown in Figure 5, the general vertical structure of the wave includes low-level convergence and upper-level divergence. On the surface, this appears as anomalously strong westerly winds behind (to the west) of the convective center and slightly anomalous easterly

winds before it. These features reverse directions on either side of the disturbance in the upper atmosphere. The surrounding large scale structures appear similar to an equatorial Kelvin wave to the east of the convective center and a symmetric pair of Rossby gyres to the west (Zhang 2005). The Rossby gyres and Kelvin waves have been described as equatorial waves forced by a localized heat

source (Yanai et al. 2000, L06). These free modes of the shallow water approximation as described by Matsuno (1966) seem to be coupled into this asymmetrical system through convective heating and zonal temperature asymmetries (Gill 1980). While these and other theories can describe some of the structure of the wave, its initiation sources need further investigation.

C. The Discharge-Recharge Oscillation

Over the past 30 years, several theories have been proposed to explain the episodic reappearance of convection associated with the MJO. In their 1993 paper, Bladé and Hartmann used a global two-level nonlinear model to examine whether the remaining circulation of one MJO, or resulting Kelvin wave, is capable of exciting the next MJO in the Indian Ocean. This would mean that the time period between the appearances of the disturbances would be dictated by the time it takes the MJO to propagate around the planet. However, their results suggested that the remains of the previous MJO were not the primary source of energy for the next wave. Instead, they found that MJO-like disturbances were generated periodi-

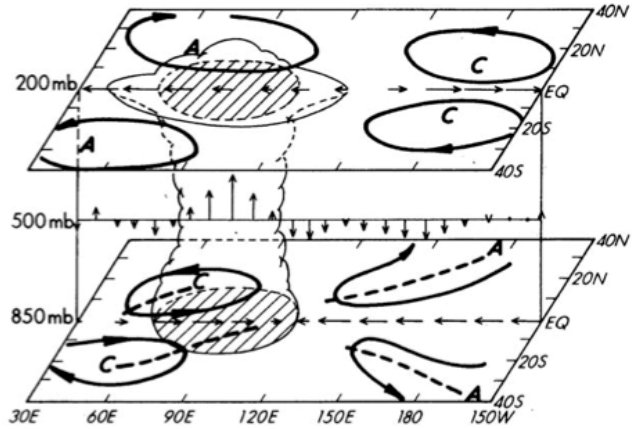


FIG 5: A simple schematic of the basic vertical structure of the convective center of the MJO (from Rui and Wang 1990). Shaded areas are regions of anomalously low OLR, arrows show low level convergence, mid level vertical motion, and upper level divergence. The letters 'A' and 'C' represent Anti-cyclonic and Cyclonic circulations associated with trailing Rossby gyres to the west of convection and moist Kelvin waves to the east.

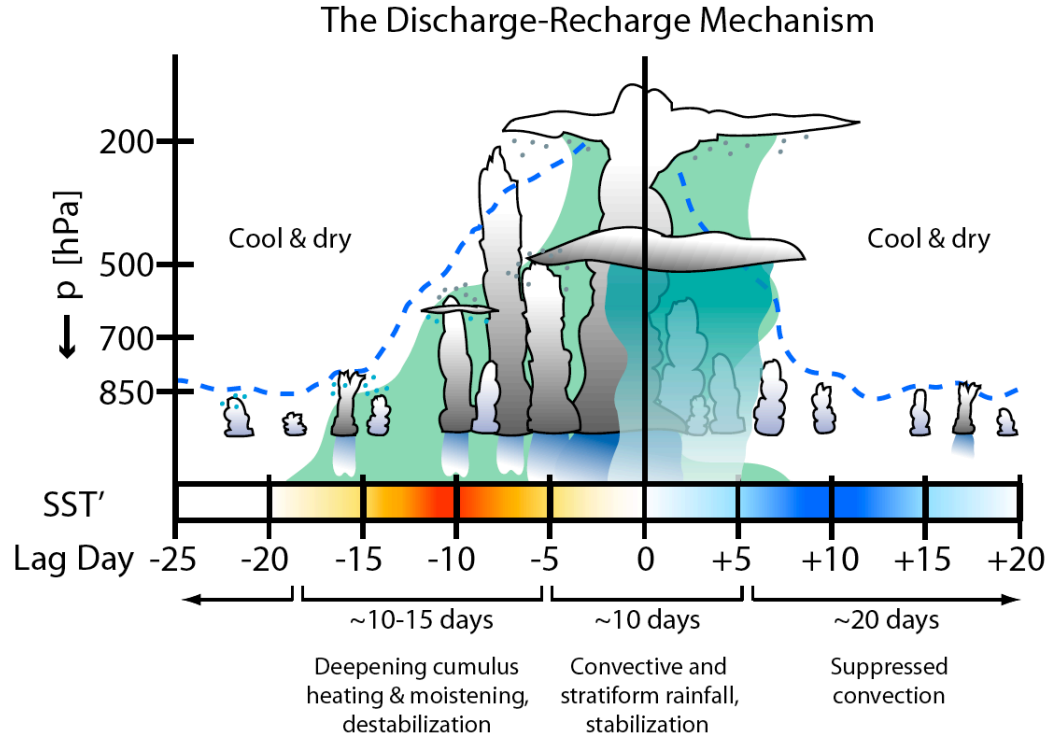


FIG 6: Illustration of the Discharge Recharge oscillation described by Bladé and Hartmann (1993) that shows the asymmetry in the MJO. It takes more time to destabilize the Indian Ocean region to its tipping point than is required to re-stabilize after the onset of deep convection. From Benedict and Randall (2007).

cally in their model purely by the local buildup of instability in the region (Bladé and Hartmann 1993). They entitled this effect the Discharge-Recharge Oscillation (DRO).

The DRO describes the MJO as an intrinsic mode of oscillation in the tropical atmosphere. Their model results suggest that the basic configuration of the Indian ocean and tropical warm pool, and the convective activity therein, are all that is necessary for an MJO to form regularly. Bladé and Hartmann present the DRO hypothesis based on the idea that convection and constant heating dictate a timescale of periodic buildup of instability as well as the timescale for the adjustment back to a stable state (through the deep convection of the MJO).

The Recharge period occurs as small and mid-scale convection slowly mix and moisten the lower levels of the atmosphere in the tropical Indian ocean. The lack of horizontal baroclinic inhomogeneities causes the building instability in the atmosphere above the Indian

Ocean basin to deepen without a local outlet for the energy. This continues until the entire region reaches the maximum destabilization that the atmospheric dynamics in the region can support, i.e., a “tipping point.” At this point, any extra-tropical forcing can cause the entire region to erupt in strong, deep, large-scale convection, and the Discharge period begins.

The convection of the Discharge period penetrates so deeply through the troposphere that it produces intense heating through all levels. In the upper levels of the troposphere, rapid condensation and precipitation formation release huge amounts of latent heat. As described above, this heating spawns surrounding Kelvin and Rossby waves. The intense convection and surrounding large-scale circulation acts to restabilize the tropical region by lifting the warm, moist air from the surface, cooling and drying through mesoscale down drafts, wringing moisture out of the atmosphere through intense precipitation, and warming the upper levels of the troposphere with latent heating. The trailing Rossby gyres help to restabilize the region by advecting in cooler, dryer, extra-tropical air behind the convection. After this discharge of pent-up tropical energy, the tropics revert to a regime of suppressed deep convection and the Recharge period begins anew.

The steps involved in this mechanism can be seen in Madden and Julian’s figure from 1972, reproduced here as Figure 3. Steps C,D,E, and F are the Recharge period, and steps G, H, A and B are the Discharge period. The DRO requires that the periodicity of the appearance of the MJO be based purely on the amount of time required to destabilize the Indian ocean and tropical warm pool region to its tipping point, and then the time required for restabilization by the MJO. The cycle produces an oscillating heat source which spawns further tropical wave activity, and dictates the phase speed of those waves (Gill 1980).

Based on this description and supporting observations, the DRO must satisfy some requirements in order to effectively grow an MJO. First of all, the basic state of the tropics must support the means for a gradual destabilization during the Recharge period, i.e., a long

period with suppressed convection and light winds. Secondly, small scale convective processes must be directly linked with moistening processes. This helps convection to moisten a deep layer of the troposphere as the tropics destabilize in the Recharge period. Local drying due to downdrafts cools the air below these smaller systems and prevents them from completely re-stabilizing the region. Finally, the Discharge period requires slightly different convective mechanisms. During this time of intense convection, the column is filled with vapor, which intensifies the convective heating through increased condensation and precipitation efficiency. The resulting strong heat source excites Rossby and Kelvin waves. The Rossby waves advect in cooler dryer air from the subtropics to shut off convection to the west, and the Kelvin wave to the east provides convergence which aids in building new convection on the other side of the heat source, and influences the convective envelope to propagate eastward. These processes are examined in more detail within the models and observations in Chapter 3.

Chapter 2: Models, Data and Methods

A. About the Models

The analysis presented here uses four years of model output from NCAR's Community Atmosphere Model (CAM) v3.0 and four years of output from the Super Parameterized CAM (SP-CAM), which were run at Pacific Northwest National Laboratory (McFarlane et al. 2007). Both versions of the model use the same Atmospheric Model Intercomparison Project (AMIP) style boundary conditions (Gates 1992), which include prescribed monthly SST, monthly sea ice, CO₂ concentration and solar forcing, for the period June 1998 through May 2002. Both versions have a GCM grid spacing of 2° latitude, 2.5° longitude and 26 layers between 992 hPa and 3.5 hPa.

This version of the CAM has a finite-volume dynamical core (Collins et al. 2004), with a dynamical timestep of 20 minutes and a radiation timestep of one hour. Deep convection, shallow convection and stratiform clouds are all simulated with separate parameterizations. The deep convection scheme is based on Zhang and McFarlane (1995). It statistically describes the effects of the mass fluxes generated by a group of deep, penetrating convective updrafts and downdrafts, or cloud plumes. The scheme is triggered when conditional instability, or convective available potential energy (CAPE), develops in the column. The effect of the plume ensemble is to lift warm, moist air from below the cloud base to the top-most level of the cloud plumes where it is detrained with the same dry static energy as the environment. The air within each updraft is diluted during ascent by entrainment. Higher

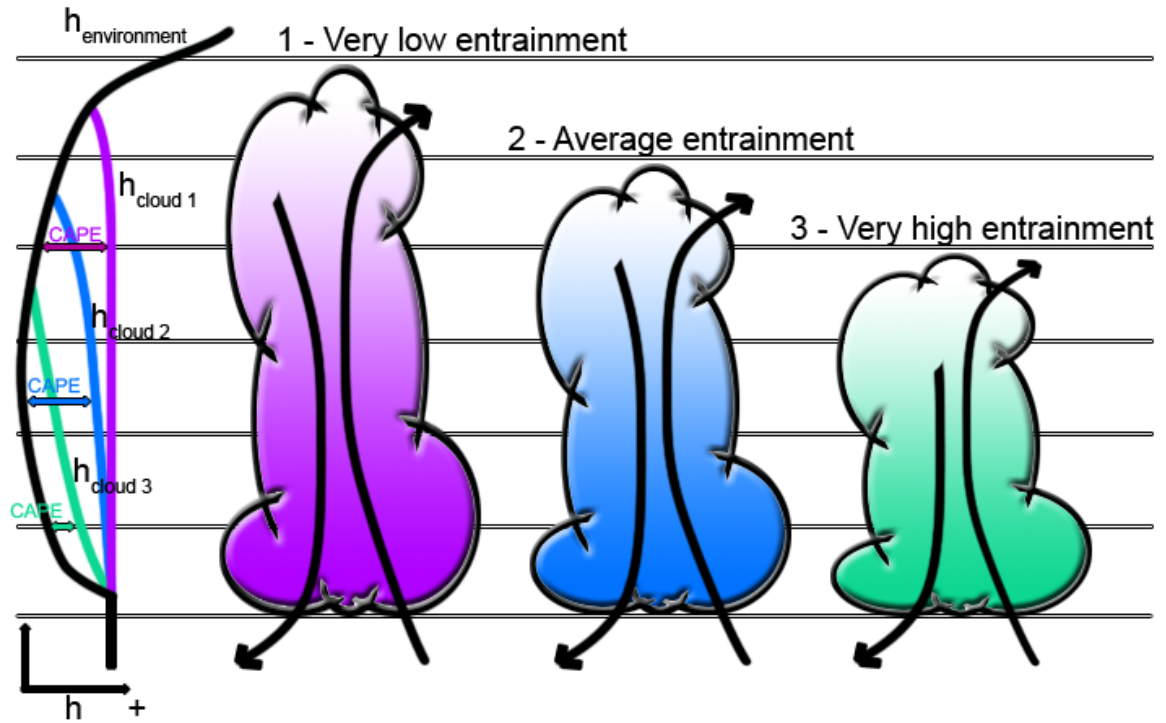


FIG 7: A brief illustration of the cloud model in the Zhang and McFarlane (1995) deep convection parameterization. Each instance of the parameterization includes an array of clouds, each with the same bottom height, but with different entrainment amounts. Due to buoyancy constraints, different entrainment values lead to different cloud top heights, but all clouds reach above the tropospheric minimum of saturation moist static energy (h). These clouds detrain mass at their tops, and downdrafts only affect the sub-cloud layer.

entrainment of environmental air results in a less buoyant parcel, and a lower height of the plume.

As the updrafts in the statistical ensemble of cloud plumes lift warm moist air from the surface, and the downdrafts cool regions below the clouds, the net effect is to reestablish stability, and destroy the CAPE which triggered the parameterization in the first place. In order to keep this realistic, a timescale is imposed on the process, which leads to an exponential decay of CAPE in the column. The local amount of CAPE and timescale required to destroy it determines the intensity of the convection. The closure condition for this parameterization is that the net mass flux at the base of the cloud must be proportional to the amount of CAPE in the column and the rate at which the CAPE is consumed.

$$M_b = \frac{A}{\tau F}$$

Here M_b is the mass flux at the uniform cloud base, A is the amount of CAPE in the column, F is the CAPE consumption rate per unit cloud base mass flux and τ is the specified timescale for the convective adjustment. In this version of the CAM, τ is generally set to 7200 seconds. This closure contains options for “tuning” the convection within the model until it behaves realistically. If the parameterization destroys CAPE too fast (resulting in too little deep convection), a modeler may simply increase τ . While the dynamics of the scheme represent realistic processes of deep convection, many of the assumptions and parameters associated with it are somewhat empirical or simply arbitrary.

Within each gridcell, all of the plumes are assumed to have the same cloud base, and all cloud tops are forced to be above the mid-tropospheric minimum of saturated moist static energy. The result is convective corrections to the column temperature profile occur only in the conditionally unstable portion. This is a representation of the actual dynamics of deep convective towers in the tropics, which rise until their updrafts lose buoyancy and generally detrain the most mass in the upper portions of the troposphere. However, this parameterization does not actually include the processes required to produce anvils and thick upper level cirrus clouds. Detrained liquid water from deep convection must be passed as a parameter to the stratiform cloud parameterization.

In this deep convection scheme, downdrafts form at or below the cloud-top detrainment layer, and are initiated by the formation of precipitation in the updraft ensemble. The amount of mass to be carried downward is calculated with a similar closure as the updrafts, described previously. However, a further constraint is placed on downdrafts: their mass flux must be proportional to the amount of precipitation and precipitation re-evaporation in the

plume, and no more than 20 percent of the precipitation is permitted to re-evaporate. Mass is detrained through downdrafts only below cloud base, so mixing via this transporting mechanism only affects the boundary layer.

This convection scheme does a good job of redistributing mass and energy in the column in order to restore large scale stability. However, the scheme is unable to realistically reproduce some tropical convective processes because of the artificial constraints described here. The scheme has difficulty moistening the middle troposphere, because detrainment is only permitted to occur above the mid tropospheric minimum of moist static energy. In the actual tropics, rain re-evaporation from anvils and mixing from convective downdrafts or the upper levels of smaller clouds can moisten air throughout the depth of a convective area. However, these processes are not represented in this deep convection scheme. Also, this scheme produces the majority of the precipitation in the model (see Figure 23), but does not produce very intense precipitation, because the power of the convective circulation is driven by CAPE, which can produce convection more often than is realistic. When convection is occurring too often, the atmosphere does not have time to increase available moisture for heavy rain events before it is rained out by lighter rain events.

The shallow convection parameterization in the CAM works to partially correct many of these issues through the introduction of the statistical effects of small scale convection in each GCM gridcell. This version of CAM uses the shallow convection parameterization described in Hack (1994). This is an extension of the moist convective adjustment scheme first described in Manabe et al. (1965) and Arakawa et al. (1969). The method divides moisture and energy budgets into convective-scale (non-resolvable) and large-scale (resolvable) terms. A cloud model is then applied, which assumes that the convective updrafts are only a small fraction of the overall area. This cloud model includes fast vertical updrafts (a cloud mass flux) like the deep convection scheme, but the shallow scheme has no downdrafts, only

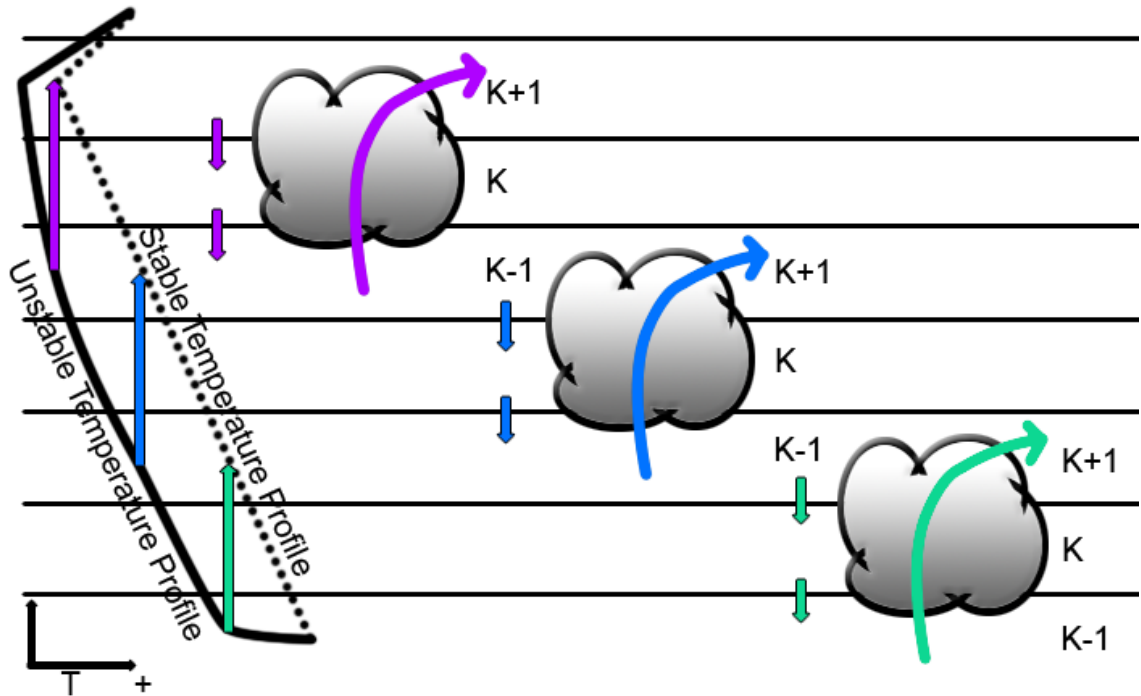


FIG 8: A brief illustration of the cloud model in the Hack (1994) convection parameterization. Environmental instability is adjusted towards a stable profile through the use of abstracted “clouds” which transport mass and energy (temperature) across three layers at a time. The mixing provided by this shallow cloud algorithm begins near the surface and iterates upwards three layers at a time. Environmental subsidence tempers the mixing, and requires more iterations of clouds (or a longer, more realistic timescale) before stability is achieved.

slowly descending air surrounding the updrafts (a residual environmental mass flux). Just as in the deep convection scheme, these approximations allow the model to determine cloud scale vertical transports in terms of the difference between the average properties of air rising in clouds and the average properties of air sinking around them.

The shallow convection scheme uses clouds which form in three layers when the column becomes moist adiabatically unstable. The clouds entrain air through their bases and detrain at their tops in proportion to their cloud mass flux. The net effect of these shallow clouds is to adjust the temperature and moisture in the nearby layers such that they are nudged back towards stability. The cloud model is applied iteratively from the bottom of the GCM column to the top, allowing these shallow clouds to adjust the profiles of energy and temperature back towards equilibrium, as well as transport mass vertically, and detrain water vapor at many levels. While this parameterization could work on its own as a general convection

scheme, the CAM uses it along side Zhang and McFarlane (1995) to add in these effects of smaller scale convection. The use of two convective parameterizations in the CAM is partly due to retaining the legacy code from previous versions of the CAM, and partly because without the Hack scheme, mid-latitude forecasting skill drops dramatically (personal communications with Richard Neale at NCAR).

Regardless, a few problems remain to be addressed. While this shallow convective parameterization is better at detraining moisture through the column, it does not include the effects of downdrafts at all. Also, this scheme is better at moistening many levels of the lower and mid-troposphere, but it does not produce much precipitation. This will produce a disconnect between intense rain events (caused by the deep convective scheme) and efficient moistening of the region (caused by the shallow convective scheme). This issue might be further amplified by the arbitrary ordering of the two convection parameterizations. The deep convection scheme runs first and reduces most of the instability. This would prevent the shallow convection scheme from being used frequently, and its moistening processes would not occur as often as necessary. Finally, neither of these parameterizations include the effects of cloud anvils, or large-scale stratiform clouds and precipitation that often surround convective towers.

It is this final problem that motivates a third parameterization of cloudiness in the CAM, this one specifically for stratiform clouds. This version of the CAM uses a form of the stratiform parameterization described in Sundqvist (1988). Unlike the previous two parameterizations, this one is only called when the air in the column is stable. This, presumably, would occur after the above convective parameterizations have finished running. If the relative humidity for a layer is above a cut-off value, the condensation parameterization is invoked. This cut-off value does not need to be 100 percent, as the parameterization allows for partly-cloudy layers. Also, the CAM allows for liquid water to detrain from the Zhang

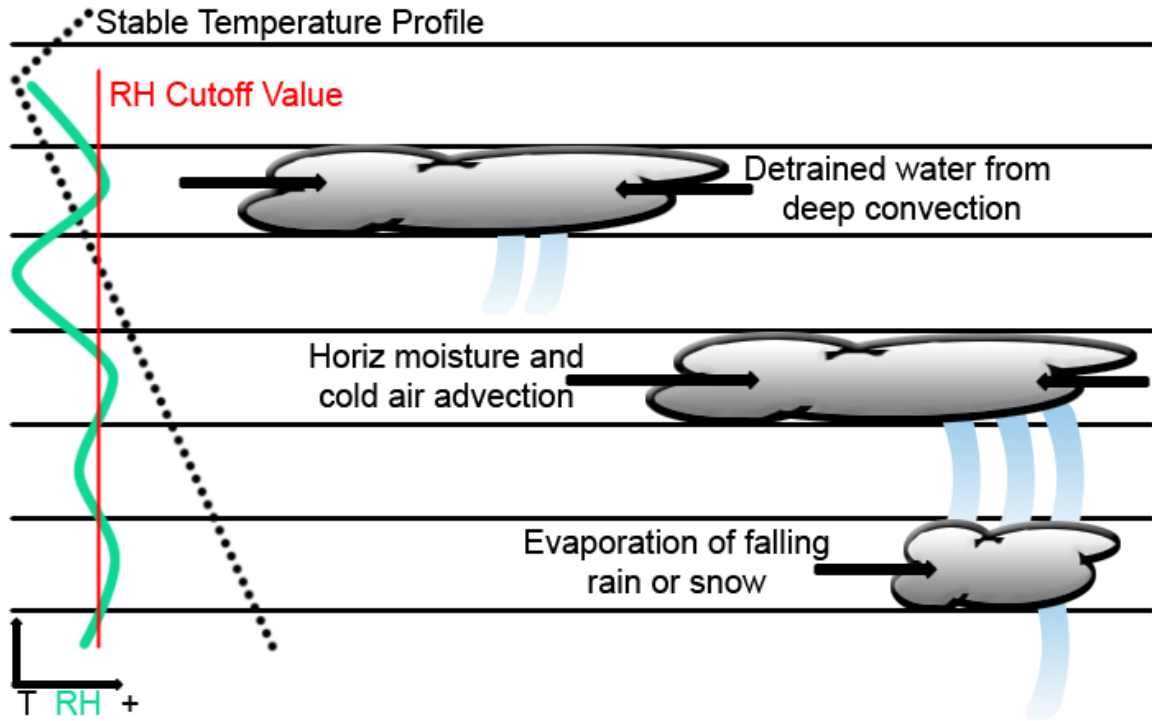


FIG 9: An illustration of the stratiform cloud parameterization in the CAM. These clouds only appear when the environment is already stable, and are generated when either the local relative humidity passes a tunable cutoff value or liquid water is detrained from the top of deep convection in the Zhang and McFarlane scheme. A number of dynamic and thermodynamic processes can affect the local relative humidity, some of which are shown here. No vertical transport of mass or energy takes place aside from precipitation processes.

and McFarlane (1995) convective towers, and this becomes an input parameter to the stratiform scheme which can also trigger the parameterization, even if local relative humidity is below the cut-off value.

The general purpose of the stratiform cloudiness parameterization is to determine the amount of grid-box averaged non-convective condensation. This is influenced by a variety of parameters, including the results of local convective parameterizations, horizontal moisture and cold air advection (but not vertical), and evaporation of rain or snow falling through the gridcell. The net condensation, in turn, influences the amount of cloud liquid water, the formation of precipitation and the localized latent heating. This is a fairly simple scheme to model the likelihood of large-scale cloud formation in the absence of convection. There is little vertical mass or energy transport (outside of precipitation processes), which

might not be accurate in the deep stratiform regions following intense convection in the tropics. Also, the coarse vertical resolution of the GCM on which this is applied will make it difficult to accurately model thin cloud layers, such as low level marine stratocumulus.

Finally, the CAM has a fourth parameterization to diagnose cloud fraction for radiation purposes outside of the three cloud parameterizations described above. Low-level marine stratus cloud fractions are diagnosed based on the profile of potential temperature between 700mb and the surface. Convective cloud fractions are diagnosed based on the updraft mass flux in each of the convective parameterizations, and all other cloud fractions are diagnosed based on relative humidity. This value of cloud fraction is very important for the radiation processes in the model, and the eventual effect of these three simple diagnostic relationships is to determine the entire effect of clouds on the radiation balance of the planet. Because of this important contribution to the energy budget within the model, it is unfortunate that the radiative effects of the clouds are not directly linked to the convection parameterizations.

The SP-CAM, in contrast, does not use statistics or large-scale relationships to simulate the effects of clouds. Each GCM gridcell contains a two dimensional Cloud Resolving Model (CRM), which solves the non-hydrostatic equations using the anelastic approximation. Details on the formulation of the CRM can be found in Khairoutdinov and Randall (2003), and more information on its implementation within the CAM can be found in Khairoutdinov and Randall (2001) and Khairoutdinov et al. (2005). The 2D CRM in each gridcell has 64 columns which are four km wide, oriented in the east-west direction, and have periodic boundary conditions. There are 24 height-coordinate levels which roughly correspond to the lowest 24 of the 26 sigma-coordinate levels in the external GCM grid (the CAM grid). The embedded CRM grid is coarser than some other CRMs, but the cost of running a finer grid is simply too high at this point in time. Also, sensitivity studies have shown little improvement with a higher resolution grid (Khairoutdinov, personal correspondence). The

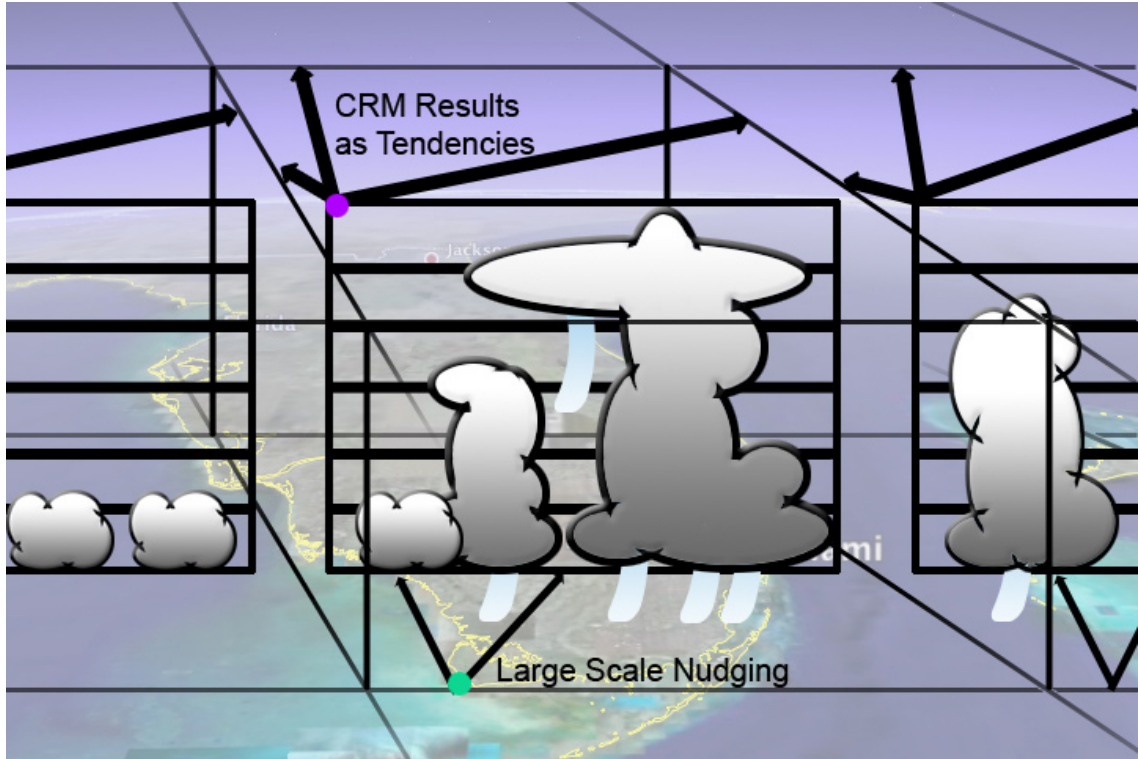


FIG 10: A simple illustration of the architecture of the Super Parameterization in the CAM. Each $2^\circ \times 2.5^\circ$ GCM gridcell contains a 2 dimensional Cloud Resolving Model (CRM) with 64 4km wide columns oriented in the east-west direction with periodic horizontal boundary conditions. The large scale GCM fields provide a constant backdrop that acts to nudge each CRM towards appropriate simulation. Conversely, the resulting cloud, moisture, and radiation fields are returned to the parent GCM as physics and radiation tendencies. Credit for the satellite image goes to NASA and Google Earth.

embedded model is being run with a 20 second timestep (60 steps for each 20 minute timestep in the CAM) in each of the 12,960 columns of the parent GCM. Depending on the computer used, the SP version of the model runs about 200 times slower than the traditional CAM.

The CRM within the SP-CAM predicts the amounts of liquid or ice-water moist static energy, the total non-precipitation cloud water and the total precipitating water. CRM fields are continuously nudged towards the GCM state, so the two model simulations do not drift apart. After each GCM timestep, the CRM returns horizontal mean fields as tendencies or results due to cloud processes in each gridcell. The CRM is prevented from transferring momentum tendencies to the parent GCM due to the unrealistic two dimensional dynamics. Radiative transfer for the SP-CAM is calculated within the CRM, and is performed

interactively for each grid column every 15 minutes. Land-surface processes, including all surface fluxes and boundary layer parameterizations, are still calculated with the traditional parameterizations on the GCM grid in the SP-CAM. This means surface effects such as increased evaporation due to resolved convective processes (gust fronts or downdrafts) are not included in this model. Also, the CRM levels in each column correspond to similar vertical levels in the parent GCM, so many boundary layer clouds and processes are still difficult for the SP-CAM to resolve. In general, the SP-CAM has the capability of doing a much better job of simulating the large-scale effects of smaller scale cloud processes, but still lacks the ability to truly simulate the actual small scale processes.

In summary, the traditional cloud parameterizations in the CAM provide a statistical method of simulating the smaller-scale effects of convection on the larger-scale GCM grid. The CAM uses four different parameterizations related to cloud effects, each of which has its own assumptions, simplifications, benefits and drawbacks (see Table 1 on the following page for a summary comparison). The SP-CAM is able to actually simulate many of the sub-grid-scale cloud processes by embedding a two-dimensional CRM in each GCM gridcell. This approach has its own benefits and drawbacks (also summarized in Table 1). A major benefit, which is of highest importance to this study, is that the convective processes in the SP-CAM are able to produce a realistic-looking MJO.

TABLE 1: Overview of parameterization assumptions and simplifications, reasoning behind each in blue.

CAM
<p>Deep Convection - Zhang and McFarlane (1995)</p> <ul style="list-style-type: none"> • All cloud bases are at a single level <ul style="list-style-type: none"> ▶Generally true with the coarse vertical resolution of a GCM • Cloud tops and all detrainment must be above tropospheric minimum in saturation moist static energy <ul style="list-style-type: none"> ▶Convection is based on buoyancy as measured by CAPE. If a parcel reaches the level of free convection it will continue to be buoyant until the environmental MSE begins to increase again. • Little updraft mixing, no lower detrainment <ul style="list-style-type: none"> ▶In a moist environment, with fast-moving and penetrating updrafts, mixing is minimal and has little impact • Downdrafts only detrain below cloud base <ul style="list-style-type: none"> ▶Somewhat accurate with coarse vertical resolution, and this deep convective scheme has no detrained cloud for precipitation formation outside of the convective tower.
<p>Shallow Convection - Hack (1994)</p> <ul style="list-style-type: none"> • Mixing only 3 levels at a time possible <ul style="list-style-type: none"> ▶Legacy restriction from Arakawa et al. (1968) • No downdrafts <ul style="list-style-type: none"> ▶Intense downdraft does not make sense on a three-level adjustment • Limited to instability left after Deep Convection scheme runs <ul style="list-style-type: none"> ▶Goal of this parameterization is to reduce left-over instability
<p>Stratiform Cloud - Sundqvist (1988)</p> <ul style="list-style-type: none"> • No vertical motion or layer mixing <ul style="list-style-type: none"> ▶Vertical motion of most clouds in a stable regime is minimal, and difficult to resolve on GCM layers • Not directly connected to other cloud schemes <ul style="list-style-type: none"> ▶Legacy of the cloud physics abstractions
SP-CAM
<p>All Convection - 2D CRM - Kairoutdinov and Randall (2003)</p> <ul style="list-style-type: none"> • CRM only 2 dimensional, with somewhat coarse 4km resolution <ul style="list-style-type: none"> ▶When limited by computational resources, this provides a good result • Periodic boundary conditions instead of one CRM connected to the next <ul style="list-style-type: none"> ▶simplifies coding, maintenance and abstraction. Produces results in the same manor as a traditional parameterization, which makes analysis a little easier • Does not provide surface fluxes to large-scale GCM (no local surface model) <ul style="list-style-type: none"> ▶Limited by computational resources • No convective momentum transport <ul style="list-style-type: none"> ▶2D CRM does not provide physically accurate momentum tendencies • Same vertical resolution as large scale GCM - poor resolution in the boundary layer <ul style="list-style-type: none"> ▶Limited by computational resources, and simplifies coding

B. Observational Data

A variety of observational data are also used in this study as a comparison basis for both models. Much of the observational tropical precipitation analysis uses precipitation rates from the Tropical Rainfall Measuring Mission (TRMM). The gridded 3B42 product is used, which gives rainrates every three hours on a $0.25^\circ \times 0.25^\circ$ grid over the tropics from calibrated IR merged with TRMM and other satellite data (see Kummerow et al. 2000 for more information). These data are then averaged to a $2.5^\circ \times 2.5^\circ$ grid to compare with the models, and averaged to daily rates. While the TRMM satellites provide a very nice, long record of tropical rainfall, this study only uses the time period of comparison to the models (June 1998 through May 2002).

A key observational resource for this study is the sounding and derived profile datasets from the Tropical Ocean Global Atmosphere (TOGA) Coupled Ocean-Atmosphere Response Experiment (COARE) project. This elaborate observational project took place on several islands and research vessels in the tropical western Pacific between November 1, 1992 and February 28, 1993. During this time period, two convective episodes associated with the Madden-Julien Oscillation passed through the observational array. The analysis presented here includes merged profiler and rawinsonde observations of temperature and relative humidity from six sounding sites (Manus, Nauru, Kavieng, Kapinga, R/V Shiyun 3 and R/V Kexue 1, See Figure 14), tipping bucket rain gauge data from the six sites, and derived column profiles of heating rates based on budget analysis of soundings in the observational array. More information on the TOGA-COARE project and goals can be found in Webster and Lukas (1992), and details on the formulation of the merged soundings are given in Ciesielski et al. (1997).

The ERA-40 reanalysis product from the European Center for Medium Range Forecasting (ECMWF) is used throughout the study as a stop-gap solution when no more direct

TABLE 2: Overview of the data used in this analysis.

Data Source	Temporal Domain and Resolution	Spatial Domain and Resolution	Notes
CAM	June 1998 - June 2002, 3 hourly averaged to Daily	16°N-16°S and 50°E-180°E, 2° lat x 2.5° lon, 26 pressure levels 992hPa - 3.5hPa	v3.0 with finite-volume dynamical core
SP-CAM	June 1998 - June 2002, 3 hourly averaged to Daily	16°N-16°S and 50°E-180°E, 2° lat x 2.5° lon, 26 pressure levels 992hPa - 3.5hPa	GCM same as CAM. Embedded CRM fields are horizontally averaged through the grid cell and temporally averaged to 3 hourly before recorded.
TRMM	June 1998 - June 2002, 3 hourly averaged to Daily	15°N-15°S and 50°E-180°E, 2.5° lat x 2.5° lon, surface values only	Gridded 3B42 product: calibrated IR with TRMM and other satellite data
TOGA-COARE	Nov 1, 1992 - Feb 28, 1993, soundings every 5-6 hours (generally) averaged to Daily	Six sounding sites between 1°N-4°S and 147°E-167°E, High frequency soundings averaged to CAM and SP-CAM vertical dimensions	Missing data omitted from all averages. Tipping bucket rain gauge data recorded per minute, averaged to Daily.
ERA-40	June 1998 - June 2002, 6 hourly averaged to Daily	15°N-15°S and 50°E-180°E, 2.5° lat x 2.5° lon, 12 pressure levels 1000hPa-50hPa	Rain data from ERA-40 replaced with TRMM

observations are available. Of course, the ERA-40 product is not technically observational data; reanalysis data are derived from a long model run which is blended with the available observational data for the period. It is, however, a great source for information on profiles of various atmospheric variables, which are intrinsic to this study and extremely difficult to observe. For more information the formulation of the ERA-40 reanalysis product, see Up-pala et al. (2005). ERA-40 datasets used in this study are on a 2.5°x2.5° grid around the globe for the time periods included in the model data (June 1998 through May 2002). The vertical resolution of these data are coarser than that provided by the models (only 12 levels,

from 1000mb through 50mb, were used in the vertical) so many of the plots in Section III are plotted on the coarser ERA-40 levels for ease of comparison.

C. Methodology

1. Regions of Interest

Our study is focused on the processes and mechanisms behind the MJO. To that end, we identified two main regions of interest for our analysis. All spectral analysis, which requires a periodic domain, uses data from the Equatorial Focus Region (EFR) which includes latitudes from 15S to 15N. The rest of our analysis is based on the MJO Focus Region (MFR) which is also latitudes 15S to 15N, but only longitudes 50E to 180E, as shown in Figure 11.

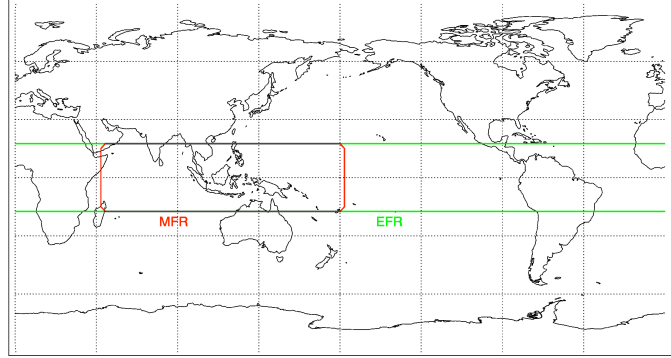


Fig 11: A map of the EFR and the MFR. The Equatorial Focus Region (EFR) extends from 15S to 15N. The MJO Focus Region (MFR) includes only longitudes from 50E to 180E and latitudes 15S to 15N.

2. Composite profiles of the tropical warm pool

A basic tool used here is a composite plot of the profile of a variable according to the rainrate in the gridcell at that time. These plots are created from all four years of daily data in the MFR. Daily average data is binned according to the surface daily average rainrate. After the sorting, all data in each bin are averaged together, and the resulting average data is plotted versus the rainrate for the bins. In this study, average vertical profiles were interpolated onto the coarser ERA-40 vertical layers to make comparison with observations easier.

3. Wheeler and Kiladis Diagrams

The diagrams exemplified by Figure 2 are very useful as an overview of the tropical wave power spectrum, and are created for each dataset generally according to the methodology

outlined in Wheeler and Kiladis (2003). First the yearly mean and first three harmonics are subtracted from the data, resulting in a time series of OLR anomalies. The asymmetric component of this dataset is determined by calculating the differences between values across the equator. This component is then divided up into a series of 96 day segments which overlap by 61 days. In four years of data, this results in 43 overlapping segments. The mean and linear trend is then removed and a tapering function is applied to each segment. This tapering function is a simple normalization factor which reduces the impact of edge values in each segment, and reduces the amount of spectral noise due to edge conditions in the Fourier transform performed next. This Fourier transform is first performed in space, and then another in time, for each segment. The power is calculated for all of the Fourier transform coefficients, and all of the segments are averaged together and smoothed to create a background spectrum. The normalized plots in Figure 2 are the result of dividing the initial average power spectrum by the smoothed background spectrum (Wheeler and Kiladis, 2003).

4. Isolation of MJO events

MJO analysis in this study is based on daily-averaged OLR in the EFR. First, the beginning and end of the data is tapered to prevent spurious spectral anomalies as is done for the segments in the Wheeler and Kiladis (2003) diagrams. However, instead of the full tapering function applied above, in this case only the first and last 10 percent of the data is tapered. This results in obscuration of any MJO events that appeared during those times, so the MJO events used in this study only occur during the middle 80 percent of the time series. The four years of tapered data is next filtered to determine the power spectrum, using a series of Fourier transforms as described previously. All power outside of waveforms which fit the description of an MJO (zonal wavenumbers one to three and periods of 30 to 70 days) is set to zero, and the process is reversed. This procedure acts as a filter, and the result is data in

the usual time-space domain, filtered to only show MJO waves. At this point, the filtered data are averaged across the latitudes into a single zonal-time index of MJO strength.

To select MJO active periods, the minimum and maximum values of averaged filtered OLR are selected from each day of zonal-time data. Days and longitudes where the minimum value lies below one standard deviation are considered areas within the ‘wet phase’ of the MJO, and days and longitudes where the maximum filtered OLR is above one standard deviation are classified as areas within the ‘dry phase’ of the MJO. The location of minimum filtered OLR for each wet phase is used as the ‘day zero’ of maximum wave intensity in composite wave passage plots. This day is determined by searching through the wet phase values of low OLR until a minimum is found, and then recording the longitude and day at that point. Maps of these locations in Figure 13 give an idea of where (longitudinally) and when MJO disturbances form in each model and in the observations. As previously shown, the CAM does not produce an MJO, but this analysis picks up

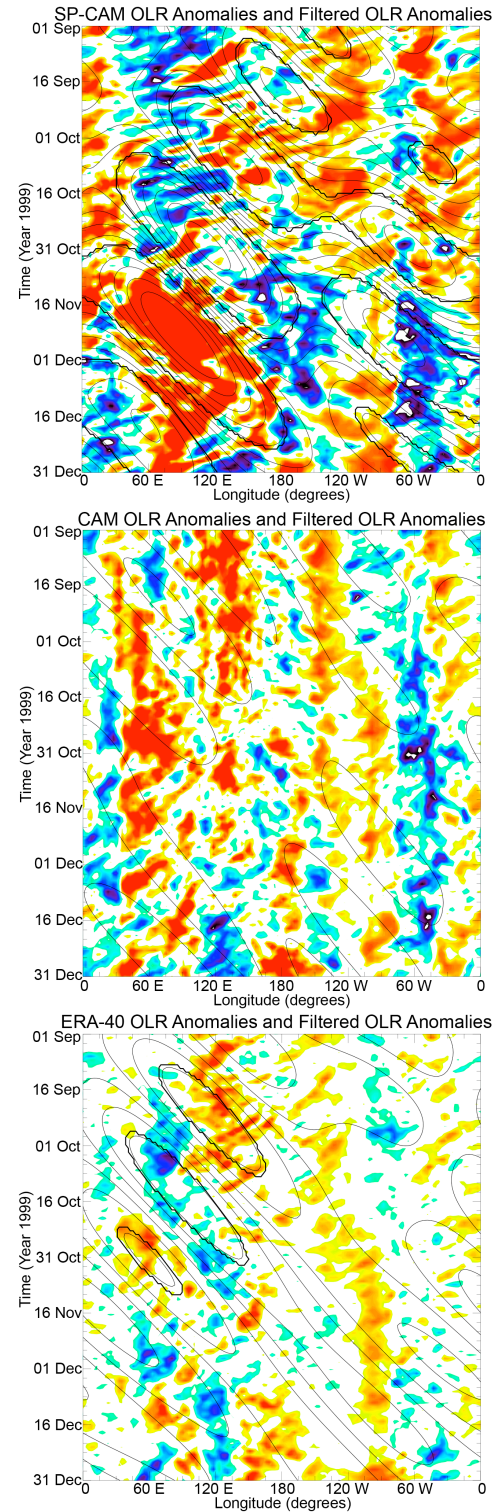
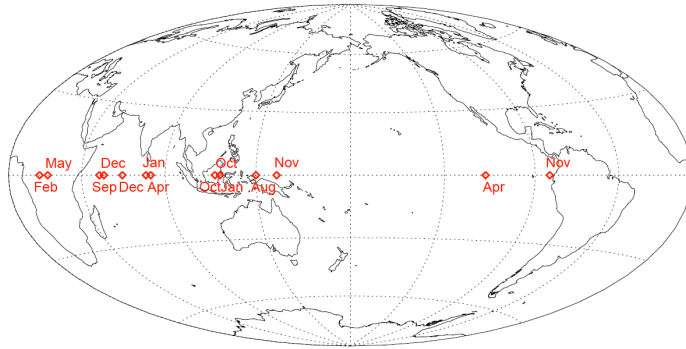
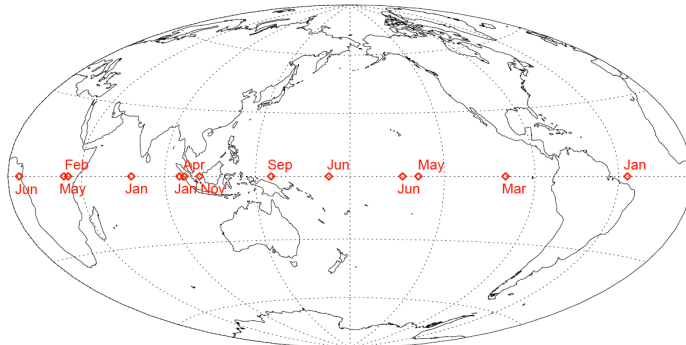


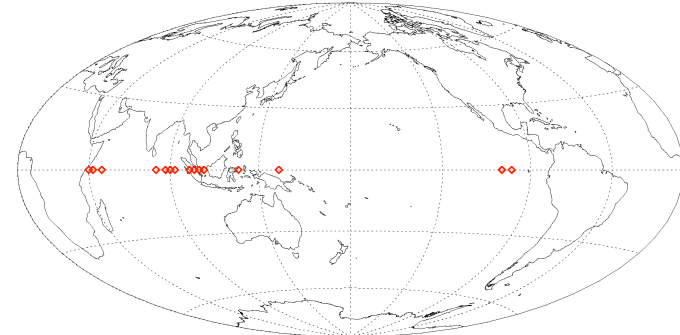
FIG 12: Time-longitude plots of OLR (color contours) along the equator. MJO filtered values (thin lines) and selected MJO events (thick lines).



Locations of Filtered OLR Minima from 6/98-6/02 (SP-CAM)



Locations of Filtered OLR Minima from 6/98-6/02 (CAM)



Locations of Filtered OLR Minima 06/98-06/02 (ERA-40)

FIG 13: Maps showing the location of the points determined to be lowest value of filtered OLR in selected MJO events. The SP-CAM (top) shows events generally in the eastern hemisphere, which is similar to the ERA-40 locations (bottom). The CAM (middle), however, shows very little geographical grouping.

13 major rain events in the region which occur with the periodicity of the MJO, and the nine found in the eastern hemisphere are used in wave composites. There are 14 identified MJO events in the SP-CAM, and 12 are found in the eastern hemisphere. For comparison, 16 MJO events are found in the ERA-40 OLR data for the same time period, 14 of which are in the eastern hemisphere.

5. Composite wave passage

After the minimum filtered OLR has been selected for each of the major MJO wet events in the data, a time-profile plot can be made at that location. A plot showing the evolution of the profile of a variable at a location on

the equator from 30 days before until 30 days after the minimum filtered OLR gives the view of the atmosphere above that point as the MJO disturbance passes over. Additionally, these evolution plots can be composited, where each day in the time series is averaged with the same day from all other MJO events. The result is a composite, or average, view of a profile of the atmosphere as the MJO approaches the point of minimum filtered OLR and after it

passes. Benedict and Randall (2007) and Stephens et al. (2004) created similar composite wave passage plots in their analyses.

5. TOGA COARE data manipulation

The TOGA-COARE data presents a highly detailed view of the tropical western Pacific atmosphere and ocean. However, the limited time and few observational points present challenges. General composite profiles (like those described in Section 2 above) are calculated based on local rain gauge data. The tipping-bucket rain data is first averaged into daily mean rainrates at each station, which are wide enough apart to allow for the approximation that each station represents the daily average rainfall of a GCM grid cell. The profile of variables for each day are then binned together in the same manor described in part one. Essentially, this procedure treats the data found at these six observational locations as six individual GCM gridcells which cover the tropical west pacific. The resulting composite profile versus rainrate plot is much noisier than those seen for longer time periods with more data available spatially, but is often adequate for comparison.

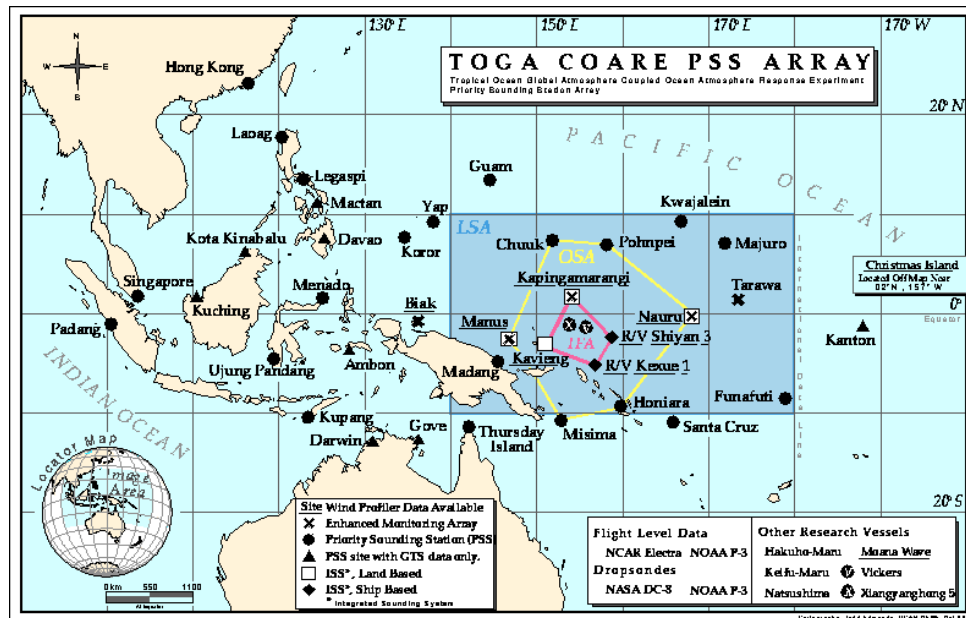


FIG 14: A Map of the TOGA COARE priority sounding sites. Data from six of the sites (Manus, Nauru, Kavieng, Kapinga, R/V Shiyian 3 and R/V Kexue 1) were used in this study. Credit for this figure goes to Paul Ciesielski.

Large-scale observational analysis has indicated that two MJO disturbances passed over the observational array during the IOP (Yanai et al. 2000). Composite plots of the wave passing over the observational array are calculated in a manner similar to that described in part five. However, the data are too sparse and too short of a time record to perform spectral analysis. Therefore, the TOGA-COARE MJO wave passage plots are centered around the first maximum rainfall at each station, which generally corresponds to the peak of convective activity found at the minimum filtered OLR in other datasets. This peak rainfall is set as the zero day for the first MJO event at each station, and then each day in the time series before and after is averaged with the same relative day at the other locations. The result is a composite view of one MJO wave passage over an array of observational points. The second MJO is not used as it occurs with atypical speed and is not as powerful as the first.

Chapter 3: Results, Analysis and Discussion

A. Large-Scale Properties of the MFR

As discussed previously, Bladé and Hartmann (1993) describe the Discharge-Recharge Oscillation (DRO) as an intrinsic mode of variability of the tropical atmosphere. This suggests that given the conditions, processes, and geography of our tropical Indian Ocean and Western Pacific on any planet or in any model, an MJO or similar large-scale eastward-propagating disturbance will occur. So our models must possess the correct basic tropical atmospheric state and representation of physical processes in order to generate an MJO. Inness et al. (2003) have also described the importance of having the correct basic state relationships in the Indian Ocean and tropical western pacific for the generation and propagation of an MJO. This section examines the large-scale state of the tropical atmosphere in the MFR of the CAM, SP-CAM, and observed tropics.

Inness specifically looked at mean winds within the tropical latitudes, and Figure 15 shows the mean zonal winds in the two models and ERA-40 data. The models are very similar in both magnitude and distribution. The most important difference is the higher magnitude and wider distribution of Indian Ocean westerlies in the mean state of the SP-CAM. This region of mean westerlies extends over the sub-continent of India and east over the maritime continent. In the CAM, the mean state over the maritime continent is light easterlies. The ERA-40 data support the results from the SP-CAM, showing light mean westerlies in the Indian Ocean and over the maritime continent. However, the magnitude of the ERA-40 average zonal wind is much less than that seen in the models. Inness et al. (2003)

showed that decreasing the easterlies in the tropical warm pool region (and especially over the maritime continent) produced a longer-lived and further propagating MJO disturbance in their model.

Several studies (Bony et al. 1997, Jakob et al. 2005) have shown that the most common atmospheric state in the tropical warm pool regions is suppressed deep convection. The top panel of Figure 16 shows that the most commonly occurring daily average value of rainrate in the MFR for the SP-CAM

and TRMM observed rainfall is also less than 0.001 mm hr^{-1} . These dry gridcells occur more than four times as often as the second most common rainrate. However dry gridcells are much less common in the CAM, and there are almost as many of them as the second most common precipitation amount, which is around 0.4 mm hr^{-1} . The CAM also has far fewer gridcells with heavy rainrates. In fact, while the other data sources have some gricells with rates that fall in the top three bins, with maximum daily average rates of above 10 mm hr^{-1} , the maximum rainrate seen in the MFR of the CAM is only around 4 mm hr^{-1} . This lower

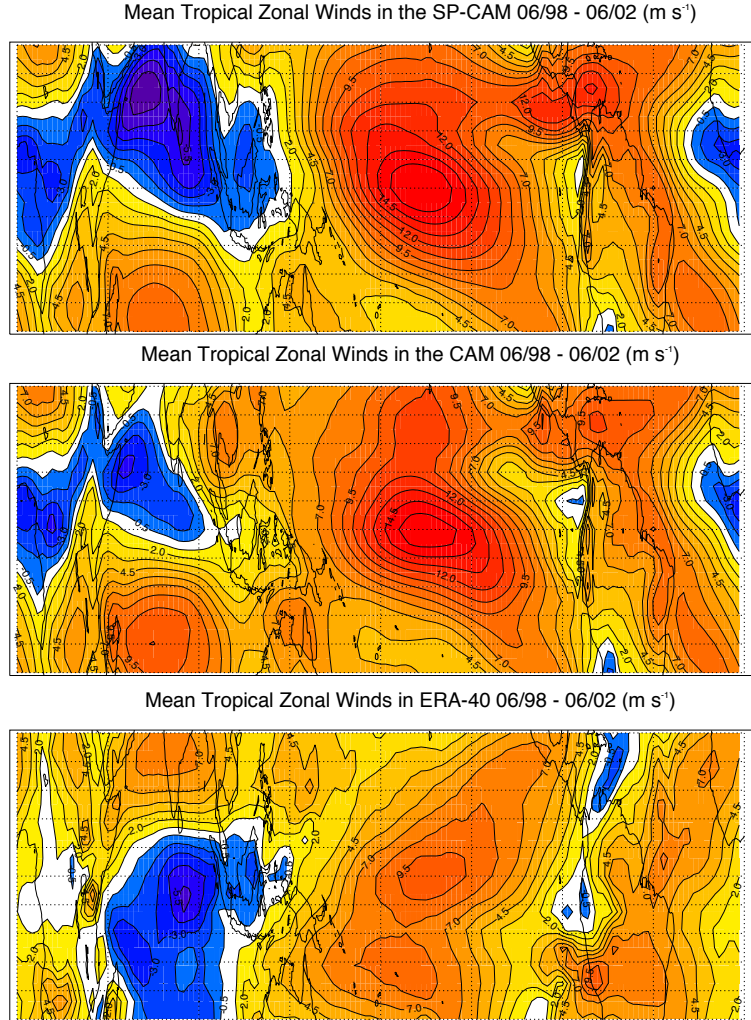


FIG 15: Maps of mean zonal winds at 850 hPa between 16S and 16N around the globe for the SP-CAM (top) and CAM (middle) and ERA-40 (bottom) during the entire four year period analyzed. Easterlies are positive and in yellows and reds, while westerlies are negative in blue and purple.

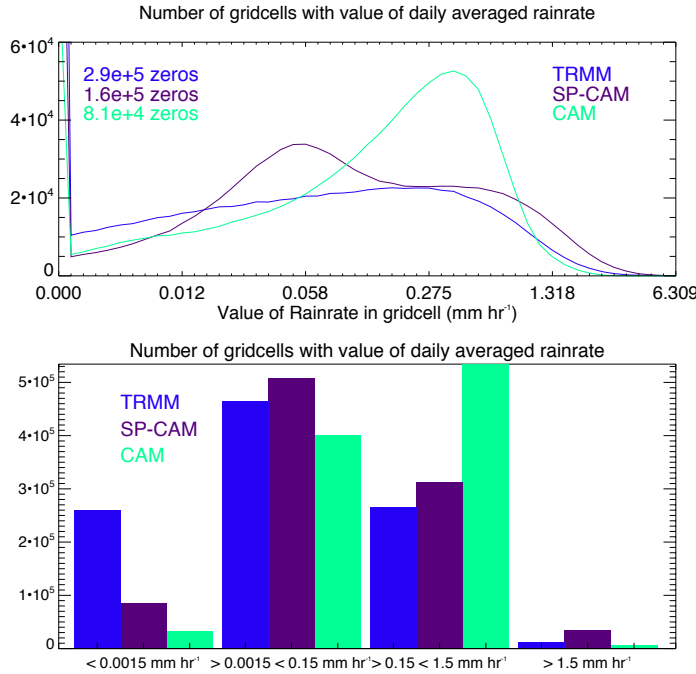


Fig 16: Histograms of gridcells with a given daily average rainrate for the four years of data used in this study. These include all gridcells in the MFR. (Top) Number of gridcells for each of the 50 bins used in the composite analysis. Gridcells with less than 0.001 mm hr⁻¹ average daily rainrate are classified as cells with no rain and counted as “zeros”. (Bottom) Number of gridcells for each of four ranges of rainrates.

CAM. Without long periods of suppressed deep convection, the Recharge period does not have time to moisten and destabilize the atmosphere above the Indian Ocean basin to a point which will trigger a powerful MJO. Also, large scale convective circulations are difficult to organize without both very heavy convection and dry periods with suppressed deep convection.

Bony et al. (1997) show that regions of large scale subsidence and convective suppression occur about 55 percent of the time. Generally, the subsidence is very weak, with the most common vertical velocity of 0 to 20 hPa day⁻¹. This regime is associated, in her work, with a lower relative humidity (around 25 percent) and generally lower cloud-tops and cloud-fractions, which indicates light precipitation in the daily mean. Figure 17 examines the vertical velocity in the two models and ERA-40 data as a function of precipitation rate. The

number of days without rain and days with heavy rain results in a much lower precipitation variability in the CAM than the SP-CAM or TRMM observations. Khairoutdinov et al. (2005) also noted the lower variability of precipitation in the CAM, and the improvement of this feature in the SP-CAM.

This describes one of the fundamental problems with the large-scale properties of the

upward vertical velocity is stronger through more of the column for heavier rainrates in the SP-CAM, and the subsidence in low precipitation days is generally weaker through the column. While the upward vertical velocity maximum is about the same per value of rainrate in both models, the profile of upward motion in the CAM is pinched, with the highest values concentrated above the freezing level near 700 hPa. This could be due to an increase in static stability just above this level in the CAM, which acts to cap convection, preventing it from rapidly lifting air below this level. We examine this phenomenon in more detail with the discussion of Figure 18.

It is interesting to note that there are **two** regions of intensely sinking air above light rain in the CAM, and a region between where the subsidence decreases, around the melting level at 700 hPa. Since warming due to atmospheric subsidence generally acts

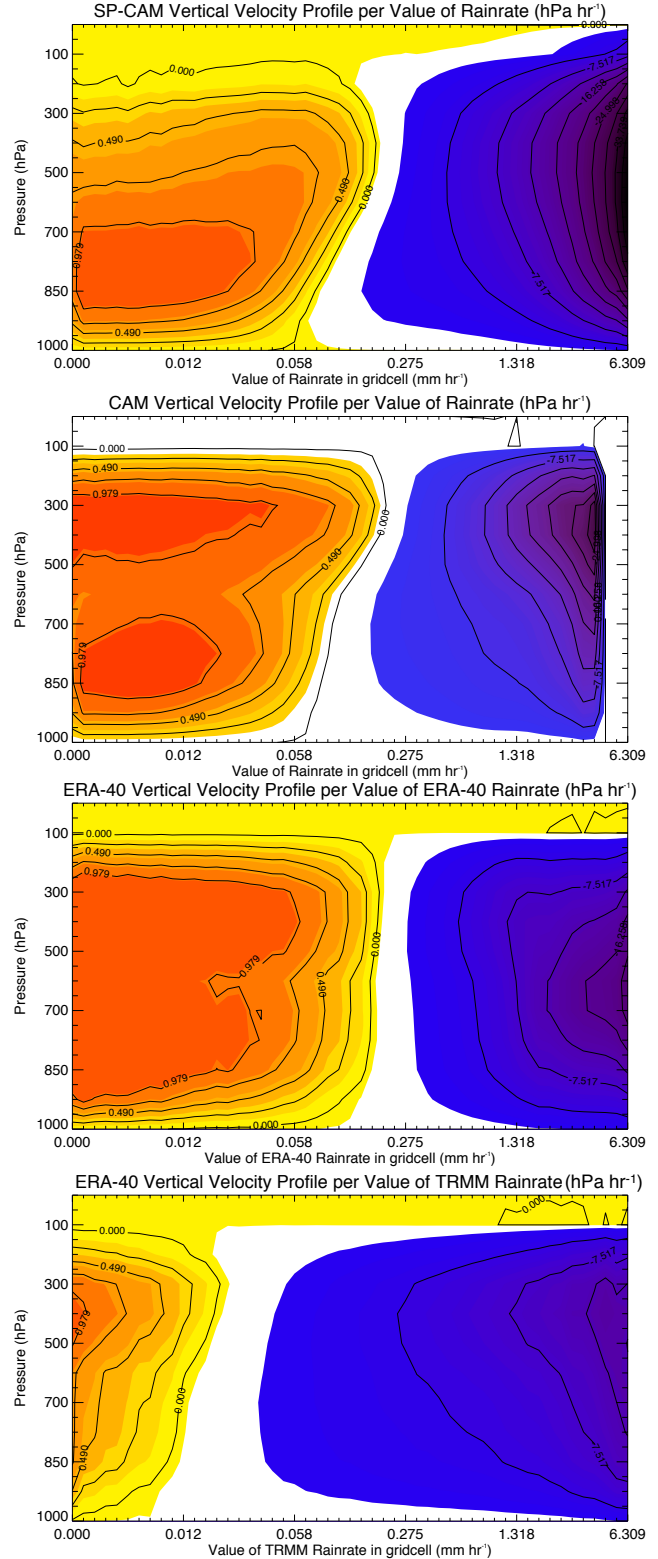


Fig 17: Averaged vertical velocity profiles for each value of daily average rainrate in the MFR of the SP-CAM (top), the CAM (second), ERA-40 with ERA-40 rainrates (third) and ERA-40 with TRMM rainrates (fourth).

to counter atmospheric radiative cooling (ARC), an increase in subsidence of the atmosphere indicates an increase in ARC in grid columns with light rain in the CAM. Plots of ARC for the two models are shown in Figure 20, and the increased cooling between 500 and 300 hPa is present in the CAM, but not the SP-CAM. ARC can be affected by a number of things, but this increase in subsidence seems to be due to a very dry region of air in this region. This extremely dry layer can be seen and will be discussed in more detail with Figure 24.

The two plots of the ERA-40 vertical velocity are interesting for a variety of reasons. The first is that this is a strong example of why we choose to use TRMM precipitation in our observational compositing rather than the ERA-40 precipitation. The plot with ERA-40 precipitation more closely resembles the distribution of velocities in the models, and has very strongly subsiding air over most of the lower precipitation rates. There is even evidence of the same bimodality as the CAM has in subsiding regions. With TRMM precipitation rates, however, most of the rainrates have rising air above them (there are fewer values of rain within sinking air regimes). This actually makes sense physically, as rain should be associated with clouds, convection, and therefore rising air. Also, it is interesting to note that the ERA-40 vertical velocity plotted against TRMM rainrates has a little bit of the same “pinched” shape in the heavy rain regions as is seen in the CAM. This will be discussed further with the moist static energy profiles in Figure 21.

A side effect of an increase in the strength of the subsidence over lightly precipitating areas is an increase in the static stability of the region. This is due to a weak inversion forming between dry air that is sinking from above and adiabatically warming, and lower level turbulently mixed air that is moistened and cooled by evaporated water from the surface. In the tropical regions this is called the trade inversion, as it is commonly associated with trade wind cumulous cloud regimes. Figure 18 examines the stability profiles in the

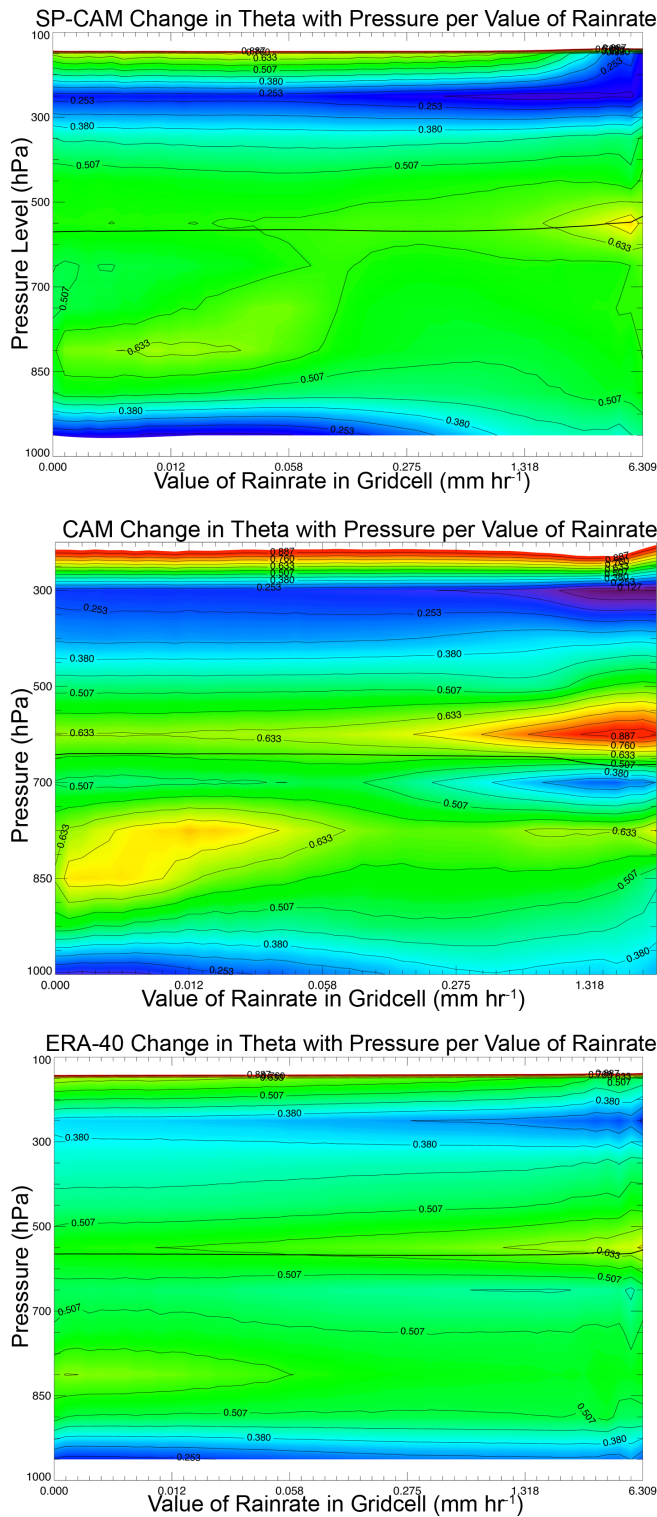


Fig 18: Averaged static stability profiles for each value of daily average rainrate in the MFR of the SP-CAM (top), CAM (middle) and ERA-40 reanalysis with TRMM precipitation (bottom).

MFR of the models and observations as functions of precipitation rate. As expected based on the vertical motion composite, the static stability above light rain events is much higher in the CAM than the SP-CAM or the observations. This tendency of the model to more forcibly resist convection during dryer periods could prevent the DRO from working correctly during the recharge period by suppressing short-lived penetrating convection which helps to moisten and condition the atmosphere in preparation for deeper convection.

The other interesting feature in the static stability figures is the region of increased stability, or temperature inversion, above the freezing level for the highest values of precipitation apparent in all three plots. This inversion is extremely strong in the CAM, with a layer of weaker stability indicated below it.

This decrease in theta below and increase above indicates a layer of very cold air right at the melting level during heavy precipitation events in the CAM. While the process of melting frozen precipitation does cool the air, this feature seems extreme, and the unrealistic cold spot is unlikely to be caused simply by melting precipitation. A further explication will be offered later in this section, in conjunction with the discussion of Figure 24.

This cold spot can be seen in the composite profile plots of potential temperature per rainrate in Figure 19. In the daily average for the MFR, the profile of potential temperature is very smooth, with little variation for different values of precipitation.

However, there is an upward bulging region for heavy rainrates in the CAM around 700 hPa, which is the cold spot. Also, for heavy rainrates in the CAM these isentropes bulge down at the top and bottom of the column, indicating heating through the column, or at least a warmer column relative to other values of rainrates in the CAM. Lower values of rainrates in the CAM have cooler potential temperatures near the surface than the SP-CAM or the observations. There is a

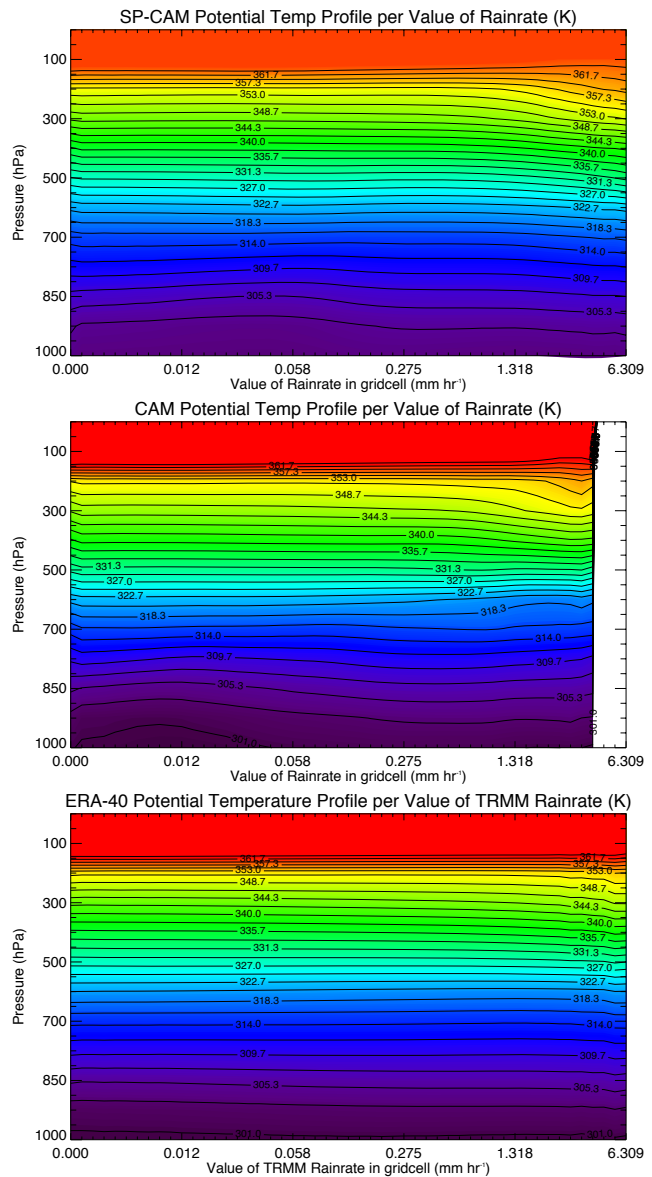


Figure 19: Averaged potential temperature profiles for each value of daily averaged rainrate in the MFR of the SP-CAM (top), the CAM (middle) and ERA-40 with TRMM precipitation (bottom).

similar general dip in isentropes at all levels for heavy rainrates in the SP-CAM, and one in the ERA-40 temperatures as well. But the ERA-40 plot is very smooth, and the dips at high rainrates in the SP-CAM seem exaggerated compared to the observations.

The warm and cold spots shown in the temperature profiles, and the vertical velocity differences between the models are all affected by the ARC, shown in Figure 20. These figures actually show cooling air with negative values, and air being warmed with positive values of ARC. In the “warmer” region with heavy rainrates mentioned in the previous discussion of potential temperature profiles, there is warming in the upper portion of the column for both the CAM and the SP-CAM. This is likely due to moist air absorbing upwelling long wave radiation. There is cooling above this warm region, where the cloud tops radiate their heat back out to space. The cooling above high rain regions of the CAM is much more in-

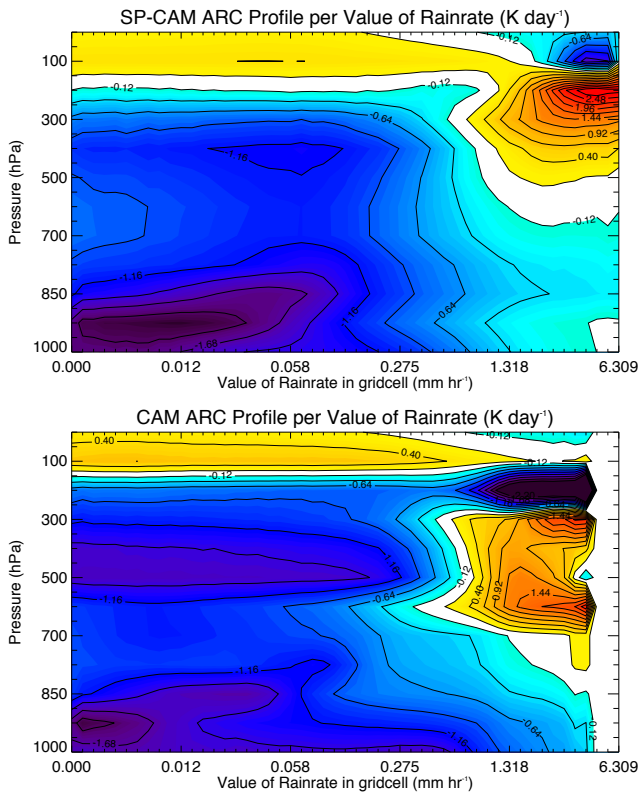


Figure 20: Averaged ARC profiles for each value of daily average rainrate in the MFR of the SP-CAM (top) and the CAM (bottom).

tense (maximum of almost 5 K day⁻¹ of cooling) than the SP-CAM (with a maximum of only about 1.5 K day⁻¹ of cooling). The location of increased cooling between 300 hPa and 500 hPa above light rain which relates to an increase in subsidence in the CAM can also be quickly picked out of Figure 20.

The increased static stability around 775 hPa for low rainrates in the CAM, however, is not as clearly linked to ARC. Figure 20 shows more cooling of near-surface air in the

SP-CAM than in the CAM. This could be related to the warmer lower level air temperatures in the SP-CAM, shown in Figure 19. The warmer air near the surface of the SP-CAM will be able to cool more than the colder low levels of the CAM. So the exact cause of the strong trade inversion over light rainrates in the CAM is still difficult to explain. It could be related to the slight tightening of isentropes above the colder surface air in the CAM. This tighter gradient between cool surface air and warm subsiding air will create a stronger inversion. This is also seen in Figure 21, where moist static energy (MSE) profiles have a very intense minimum above low rainrate gridcells.

Average profiles of MSE are shown in Figure 21. These are extremely important for the deep convection parameterization in the CAM. This parameterization is only allowed to detrain above the minimum of saturation MSE (which would be slightly higher than the minimum of actual, or non-saturated, MSE plotted here). In the intensely precipitating columns, the minimum of MSE is around 700 hPa, which is an important level in the CAM and in the discussion here. In Figure 17, the upward vertical velocity

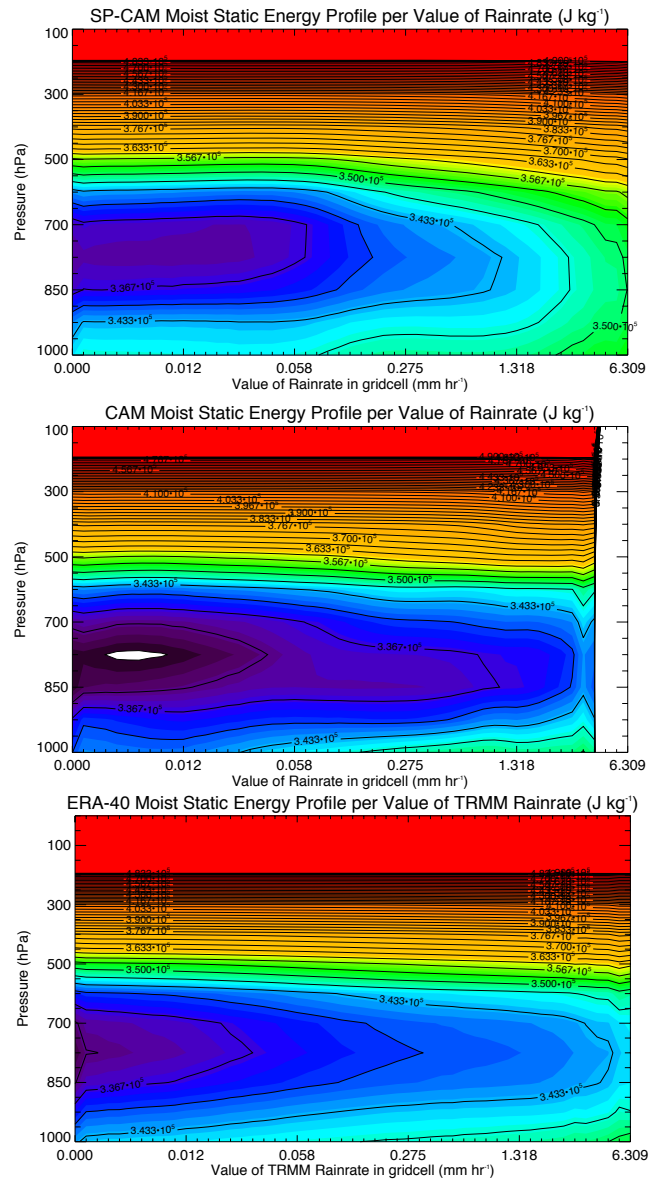


Figure 21: Averaged moist static energy profiles for each value of daily averaged rainrate in the MFR of the SP-CAM (top), the CAM (middle), and ERA-40 with TRMM precipitation (bottom).

is weak through 700 hPa, in Figure 19, the cold bulge in potential temperature occurs just above 700 hPa, and, because of this, static stability decreases right at 700 hPa in Figure 18. As we continue our discussion of tropical convection in the two models, this level will continue to re-appear as a boundary between deep convective transport and low level mixing which produces unrealistic profiles in the heaviest regions of convection. The SP-CAM does not have this artificial detrainment boundary on deep convection, and profiles above heavy rain events in the SP-CAM tend to be more vertically continuous than those of the CAM.

The highest values of rainrates in the SP-CAM have a different shape to their MSE profiles than the same values in the ERA-40 plot. In the SP-CAM, MSE has very little minimum around 700 hPa at all. It is well mixed through the column. The ERA-40 profile still contains an obvious minimum, even for the highest values of rain. This is likely the reason for the very slight pinch in vertical velocity profiles seen in the observations of Figure 17. The buoyancy argument used in the deep convection parameterization of the CAM is valid, and the ERA-40 results lend it some support. However, the constraint is so strictly enforced in the CAM that its effects are magnified out of physical proportion, and a variety of side effects and problems arise as a result.

B. Convective Moistening and Drying

Another important physical relationship which must be accurately simulated is the connection between precipitation and moistening. As mentioned many times previously, the CAM parameterization that produces the most precipitation has difficulty in moistening the column because it is constrained to detrain only above the column minimum of saturation moist static energy. Figure 22 demonstrates this lack of column vapor with a plot of the average value of total precipitable water (TPW), or total column water vapor, in the column as a function of rainrate in the gridcell. The amount of vapor in the column is less in the

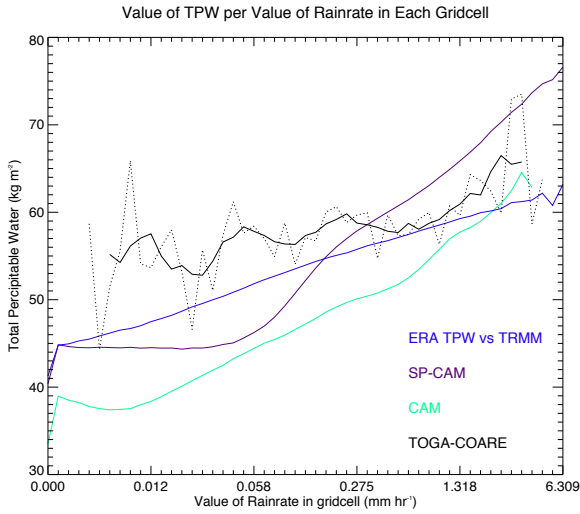


Fig 22: Averaged value of Total Precipitable Water (TPW) or total column wvapor for each value of daily averaged rainrate in the MFR.

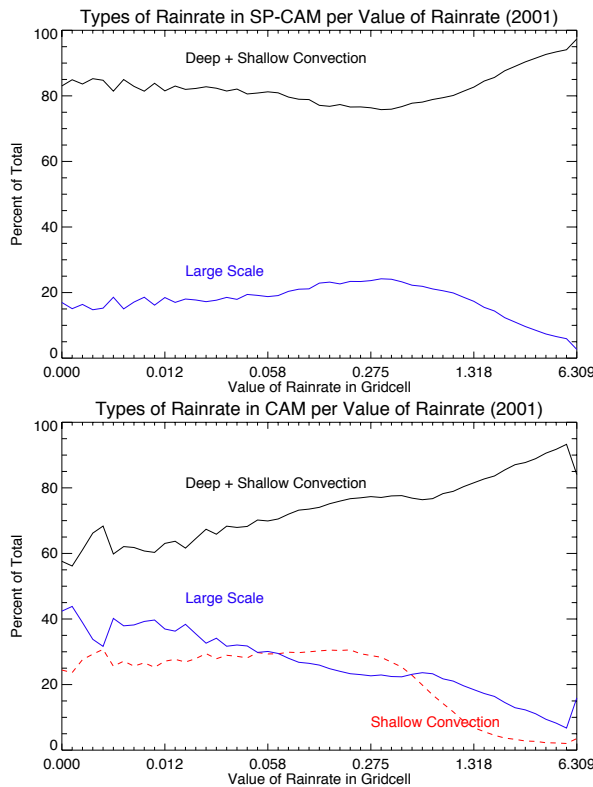


Fig 23: Percentage of daily averaged rainrate attributed to each of the three precipitating parameterizations in the CAM per value of daily average rainrate in the MFR for the SP-CAM (top) and the CAM (bottom). In the SP-CAM, the precipitation is separated into “Convective” and “Large Scale” through an arbitrary cutoff value around 10 mm/hr. Deep and Shallow convection are combined within the black line for ease of comparison.

CAM than the SP-CAM for all values of precipitation. Both models seem to be a bit too dry for low values of precipitation as compared to the observations, but only the CAM is dryer for heavier rainrates, the SP-CAM is too moist for these heavily precipitating gridcells.

We take a quick look at the sources of precipitation in Figure 23. In the upper panel, the convective and large scale precipitation are separated in the CRM of the SP-CAM based entirely on the rainrate in the CRM column. If this rainrate exceeds 10 mm day^{-1} , it is considered convective precipitation, otherwise it is classified as large-scale. Most of the rain in both models is classified as convective. In the CAM, lower rainrates are almost evenly split between convective and large scale, the SP-CAM sees a dominance of convective precipitation at all rainrates.

The CAM also has a third precipitation source which is included for reference. The shallow convection scheme (Hack 1994) does not produce much

precipitation, and the percentage of contribution dips dramatically for heavier rainrates.

We have repeatedly pointed out the disconnect in the traditional CAM between intense CAPE-driven convection in the Zhang-McFarlane scheme and the ability for the model to moisten lower layers of the troposphere. This problem is very obvious in Figure 24. These four plots show composite profiles of relative humidity per value of rainrate in the MFR for four different data sources: the SP-CAM, the traditional CAM, the ERA-40 reanalysis profile of relative humidity plotted against TRMM rainrates and the TOGA-COARE relative humidity soundings plotted against local tipping bucket rainrates. Several important differences between the two models and the observations are immediately apparent. To begin with, the CAM has a very dry layer below about 700 hPa and just above the boundary layer for all

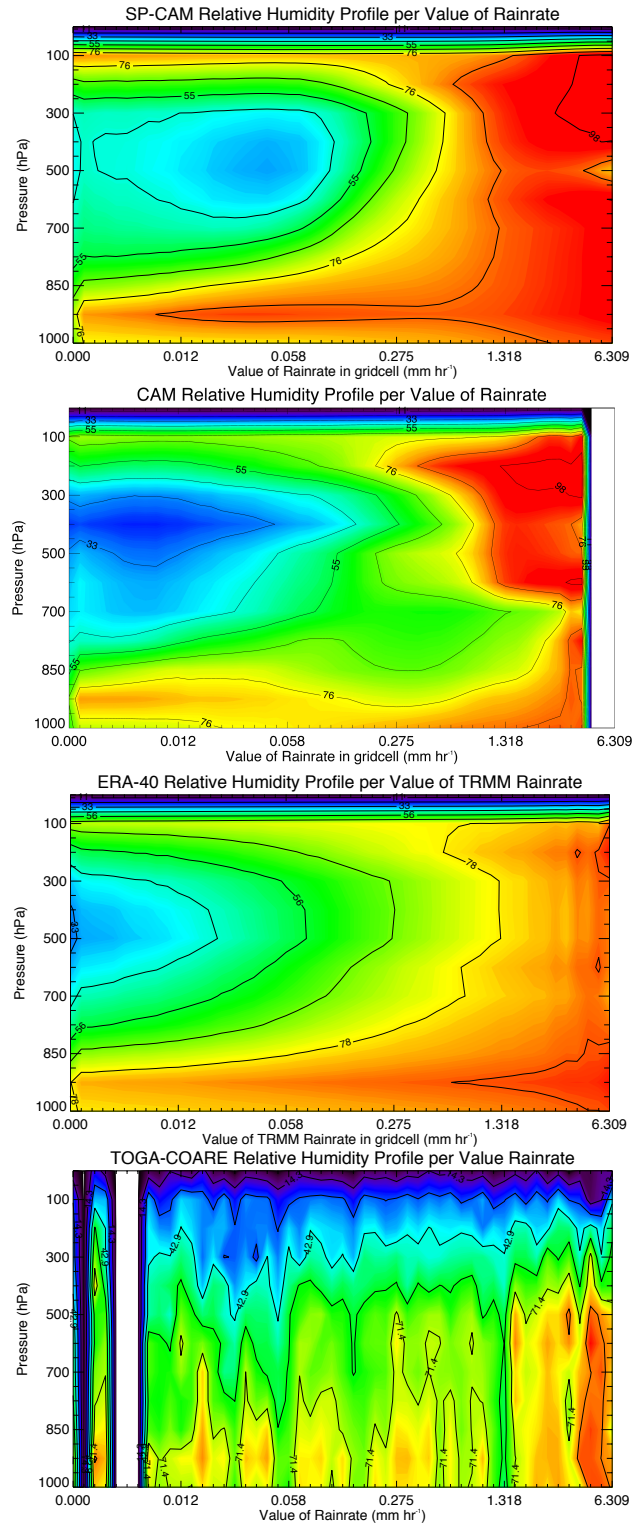


Fig 24: Composite profiles of relative humidity for each value of rainrate in the MFR for the SP-CAM (top), the CAM (second), ERA-40 reanalysis with TRIMM rainrates (third), and TOGA-COARE data (bottom).

values of rainrates. This is especially evident for heavy rainrates on the right side of the plots. Where the SP-CAM has a column of nearly saturated air above all rainrates above about 0.5 mm day^{-1} , the CAM has dry air for all of the heaviest rainrates below 700mb.

As anticipated by previous discussions, this layer of dry air can be explained by a major shortcoming in the convection parameterizations of the CAM. The majority of rainfall from almost all precipitation events in the CAM is a result of the Zhang-McFarlane deep convection parameterization, as shown in Figure 23. This scheme is artificially prevented from detraining below the minimum value of saturation MSE in the troposphere, so high relative humidity is seen mainly above this level (which is shown to be around 700 hPa in Figure 21), and the dry layer seen in Figure 24 develops.

This dry layer near 700 hPa also helps explain the intense cold spot during heavy precipitation in the CAM discussed in the previous section and shown in Figure 18 and Figure 19. As frozen precipitation falls through the melting level, it changes into rain, which cools the region. But the rain then enters a layer of much dryer air, and some of it evaporates at this point. That evaporation adds to the cooling, and the large cold spot above the heavy rain in the CAM forms.

The SP-CAM is not perfect either. The observational plots on the right side of Figure 24 show that the atmosphere should only see a fully saturated column above the heaviest rainrates, and that the layer of higher relative humidity extending to nearly 500 hPa (or higher) for middle intensity rain events should not be completely saturated. The ERA-40 and TOGA-COARE plots indicate that the very moist column for middle to higher rainrates in the SP-CAM is probably excessive.

The composite profiles in Figure 24 provide a more detailed glimpse into the relationship between moistening and rainfall than was first shown in Figure 22. Both of these figures show that rainrates should increase with increasing amounts of vapor, but do not

indicate if the precipitation is causing the increase in vapor or if the increase in vapor leads to higher rainrates. Figure 25 gives insight into this puzzle. In the SP-CAM, low values of rainrates are associated with a slight decrease in column vapor, but middle to upper levels of rain are associated with

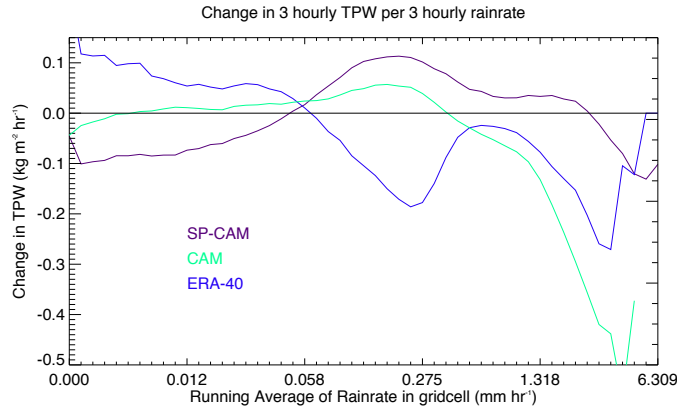


Fig 25: Change in TPW between three hourly averages composited by the corresponding six hour running mean of precipitation.

increased vapor in the column. The highest values of rainrates produce a larger decrease in column vapor. The ERA-40 analysis, using ERA-40 rainrates in this case, has a nearly opposite relationship, with the lowest values of rainrates linked to increased vapor in the column and all rainrates above 0.05 mm hr^{-1} are associated with decreases in total column water vapor. So, despite the fact that the column is drying due to precipitation formation, there is an increasing amount of vapor in the column with rainrate in Figures 22 and 24. This leads to the conclusion that heavy rain events occur after the column has previously been primed and moistened by lighter rain events.

The column moisture budgets are examined in Figure 26. For each value of rainrate the daily average evaporation, precipitation and change in TPW are plotted. The daily accumulation of precipitation curves are all the same, as they are calculated directly through the daily average rainrate which is used as the horizontal axis. The change in TPW plots are for daily rather than 3 hourly values this time, and all three plots show a similar pattern on this time scale. All three plots show drying for the highest values of rainrates, with the SP-CAM having the highest drying rate on the daily timescale. The SP-CAM and observations both show moistening for lower rainrates, but the CAM has mixed or no real change in TPW in

this region. The intense drying for low and high rainrates for the CAM in Figure 25 indicates that when there is rain in this model, the column dries out very quickly. This would explain why the lighter values of rain are not producing a distinctive moistening on the daily

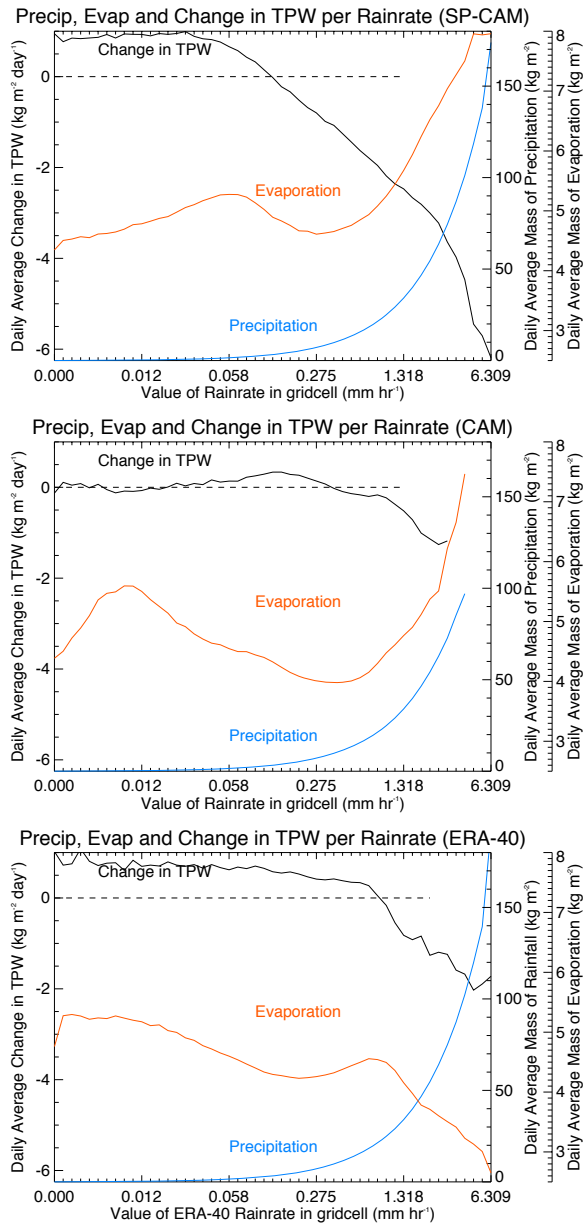


Fig 26: Composite profiles of the components of the local moisture budget (evaporation, precipitation and change in total column vapor) for the MFR of the SP-CAM (top), the CAM (middle) and ERA-40 reanalysis (bottom). In this case, the ERA-40 variables are plotted against ERA-40 precipitation in order to maintain the integrity of the budget analysis.

timescale; the effects of light and heavy rain cancel in the daily mean of the CAM.

The most obvious difference between the three plots in Figure 26 are the evaporation lines. Where the two versions of the CAM have increasing evaporation, the ERA-40 data show a decrease in evaporation with increasing precipitation. As all three models use parameterizations for evaporation based on the bulk aerodynamic formula, it is surprising that they would differ so dramatically. However, Figure 27 explains the discrepancy. Surface wind speeds are a large part of most bulk evaporation formulations, and both the SP-CAM and CAM show an increase in surface wind speeds with increasing rainrates. This makes sense on a local scale, but on the daily average over a GCM gridcell, the vertical motion of the convection should slow down the large-scale winds. As mentioned previously, the

SP-CAM uses the same surface parameterizations as the CAM, and does not feedback CRM momentum to the GCM, so the large scale surface winds ignore convective momentum drag.

The ERA-40 and TOGA-COARE surface windspeeds are included for comparison. Both observed wind speeds show little dependence on rain in the region, with a possible decrease for high rainrates. The TOGA-COARE surface winds are much lighter than those of the model, and this is possibly due to the fact that the TOGA-COARE observational period occurred only during the boreal winter (November-February). Also, the other three lines include averages from the entire MFR (50 to 180 degrees longitude, see Figure 11), which includes longitudes in the Somalian Jet region of the Indian Ocean. The TOGA-COARE observations were taken only in the western Pacific (Figure 14), which has lower mean winds (Figure 15).

This increase in evaporation with increasing precipitation could lead to a feedback in the models which would result in excessive rain events. As precipitation attempts to dry out the nearly saturated column during heavy rain events, the strong low level winds evaporate more surface moisture, and counter-act the

convective drying. The continuing low level moisture convergence feeds the convection, causing it to strengthen rather than dry out and weaken. In the CAM, the increasing evaporation problem is balanced by a more efficiently drying convective scheme (as seen in Figure 25) and deep convection does not run out of control. In the SP-CAM, without momentum feedback to

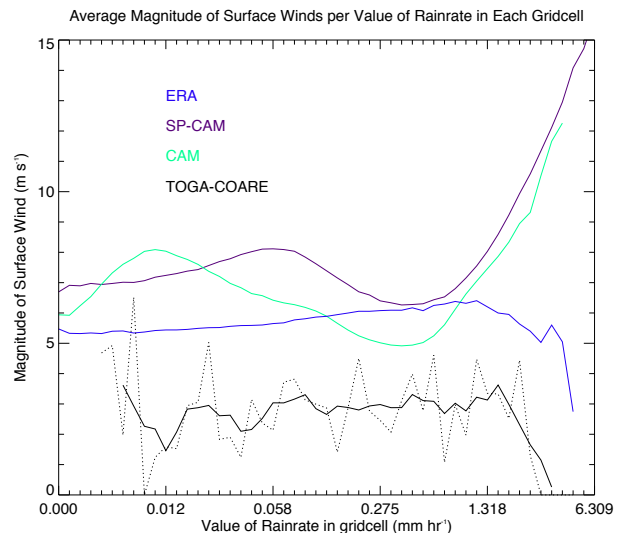


Figure 27: Composite plot of surface wind speed per value of rainrate for the MFR of the SP-CAM, the CAM, the ERA-40 reanalysis, and TOGA-COARE data.

the large-scale, the convection must be very powerful to overcome the increasing low level convergence, and the final result is deeper, stronger tropical convection occurring more often than what is seen in the observations.

This convection-wind-evaporation feedback was described in a GRL paper by Luo and Stephens (2006). Their study showed that unrealistically enhanced precipitation in the SP-CAM was associated with increased wind speeds and increased evaporation, especially in the western Pacific during the Asian monsoon periods. They ran two experiments which attempted to cutoff this feedback in the model, and both experiments resulted in greatly reduced convection and precipitation in what we call the MFR region. These experiments highlight not only the importance of evaporation to moisten and prime the environment for convection, but also the link between intense convection and a very moist environment. In their second experiment, only monthly mean evaporation from the CAM model run was used in the SP-CAM. This reduced the domain-mean moisture supply by about eight percent, and resulted in almost no precipitation in the western Pacific.

Our analysis shows that heavy precipitation should occur in a deeply moistened environment, primed by shorter lived and less intense rain. This is the case for the SP-CAM and ERA-40, which have a high relative humidity and large TPW for high rainrates, and show increasing TPW with low rainrates. The CAM has a dryer column for heavy rain rates, with most of the vapor trapped above the minimum of saturation moist static energy at 700 hPa, because of the arbitrary constraints that are part of the deep convection parameterization. The column is also dryer because the shorter time scale rain dries out the column much faster than is seen in observations or the other model, with lower rainrates resulting in little net moistening on the daily timescale. The results presented here also show that evaporation seems to have less impact than precipitation on the change in TPW when plotted against a logarithmic rain scale. However, both the CAM and the SP-CAM have unrealistic increasing

evaporation during heavy rainrates because the large-scale surface winds actually increase with increasing rain. This causes a positive feedback leading to very intense convection in the SP-CAM, but is counter-acted by the very efficient precipitation drying in the CAM. In the next section, we will show how the moist processes investigated here affect the DRO and the MJO.

C. The Discharge-Recharge Oscillation

The DRO, as described in previous sections, is a cycle of stability transforming to instability, leading to deep convection, which leads to stability eventually growing again towards instability in the tropical warm pool. The recharge period encompasses the time during which shallow and short-lived deeper convection slowly moisten and destabilizes the atmosphere. We have shown the importance of both large-scale and convective-scale properties and processes such as mean low-level winds, the frequency of occurrence of dry days and heavily raining events, and the strength of static stability during the low-precipitation regime to the recharge period in the previous sections. The discharge period then encompasses the passage of the extremely deep and powerful convection associated with the MJO. This strong convection excites a large scale circulation, and brings the region back to a suppressed state. The final section of this chapter will examine the processes important to this period. This section examines the changes that occur as the recharge period transitions into the discharge period.

The effect of the important relationship between moistening and rainfall from convective events has been seen in many ways already in our study, but its impact on the MJO and the DRO begins to appear in Figure 28. This figure shows the composite profiles of relative humidity for each of the selected MJO or strong convection events in the models. Time increases to the right, so the time before the point of minimum filtered OLR (as determined in Section 2c) is on the left hand side, and the days after on the right. The early

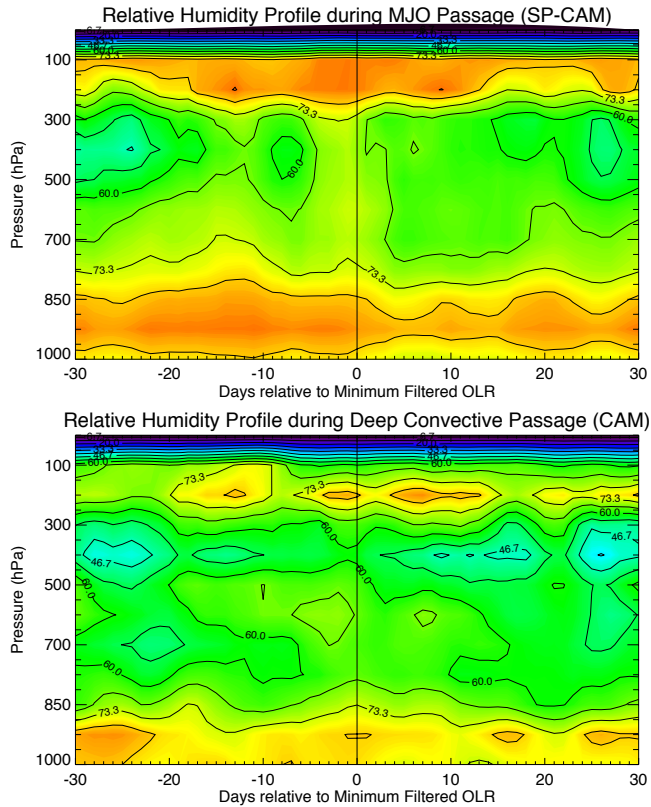


Fig 28: Composite plots of the vertical profiles of relative humidity with respect to time before and after the passage of an MJO or strong rain event in the SP-CAM (top) and the CAM (bottom).

As the MJO approaches the point of minimum filtered OLR in the SP-CAM, a thick layer of moisture forms through the lower troposphere and all the way up to nearly 700 hPa. As the heaviest convection passes, the entire column sees a higher than normal relative humidity. After the passage of the wave, the lower layer of moisture dries out, and is pinched, as dryer air arrives near the surface and top of the layer. Upper level moisture persists for several days, but gradually dissipates in the model.

The CAM, on the other hand, does not build up a thick lower layer of high relative humidity air. At the point of heaviest convection near day zero, there is the hint of an increase in relative humidity through to nearly 500mb, but, in general, the column is much dryer than what is seen in during the passage of an MJO in the SP-CAM. So this basic disconnect between precipitation and convection prevents the build up of moisture and instability during the recharge period in the CAM, and prevents the recharging process from

days of this plot could be viewed as the recharge period, and the days around day zero and immediately after as the discharge period. The recharge period begins again in a suppressed regime around day +15 and the cycle repeats.

As the MJO approaches the point of minimum filtered OLR in the SP-CAM, a thick layer of moisture forms through the lower troposphere and all the way up to nearly 700 hPa.

As the heaviest convection passes, the entire column sees a higher than normal relative humidity. After the

transforming a large-scale stable regime into one of deep instability and powerful convection.

Figure 29 further shows the impact of this disconnect on the DRO in the CAM as compared to that in the SP-CAM and observations. Each of these figures shows the evolution of the cycle plotted as a composite series of days, similar to Figure 28. However, in this figure, each day is plotted as point on rainrate versus TPW axis for the daily composite. The cycle is then smoothed with a 13 day running mean to produce the most basic shape of the DRO. The cycle is pretty clear for both models, with rainrate and total precipitable water slowly increasing during the recharge period and then decreasing during the discharge period.

The increase in TPW and rainrates seems to be closely linked in the SP-CAM and observational plots, as they both increase together nearly linearly. The TOGA-COARE MJO cycle

Smoothed TPW per Rainrate for Composite Passage

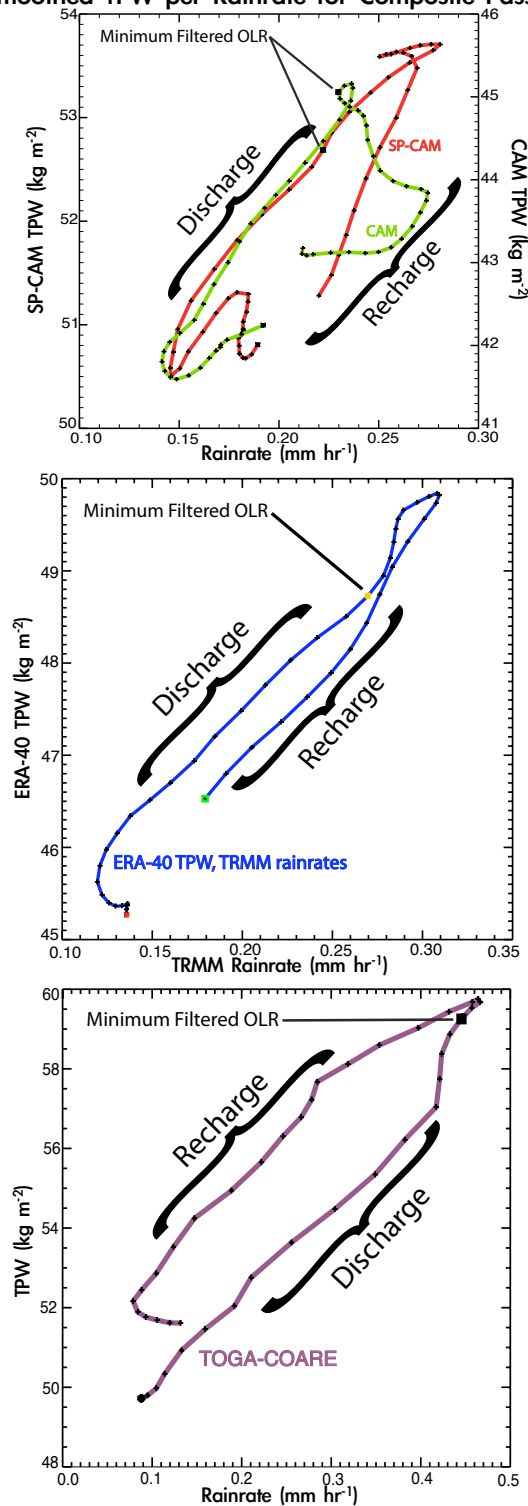


Fig 29: The cycle of Discharge and Recharge in the CAM and SP-CAM (top), ERA-40 and TRMM (middle) and TOGA-COARE (bottom). These plots are composites of the days before and after minimum filtered OLR at each point, plotted against the rainrate and TPW for each day.

actually follows the opposite direction in the figure, but the relationships between TPW and rainrates are nearly linear during the oscillation. The CAM however, begins with rainrates increasing with little moisture increase, and then hits a point where rainrates begin to decrease while TPW is still increasing. This could be due to the heavy convection occurring during these periods, and rain evaporating through the dry layer described above before it has a chance to hit the ground. Thus surface precipitation would decrease as column vapor increases at that time.

Another way to view this oscillation is presented in Figure 30. This shows the precipitation, OLR, and TPW as the MJO wave approaches the location of minimum filtered OLR

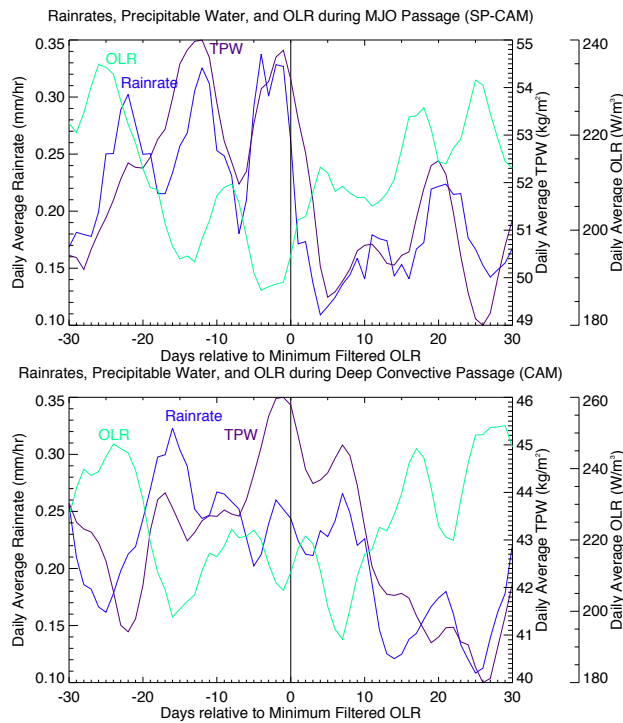


Fig 30: Composite plots of the precipitation, OLR and TPW during the passage of the MJO.

for each of the models. In our analysis, the SP-CAM shows an overall increase in precipitation and column integrated vapor over the 30 days before the wave approaches. At the same time, the TPW is also increasing, and OLR is decreasing. Similar plots were made using TRMM derived observations of several MJO events in Stephens et. al. (2004). Their plots show similar increases in rainrate and TPW before the passage and drops in the quantities after the passage of the disturbance. The CAM increases in precipitation and increases in TPW are not as well correlated, and the precipitation actually peaks well before the TPW does in this composite plot. These poorly

correlated fields produce the unrealistic DRO cycle in Figure 29, and prevent the recharge period in the CAM from properly transitioning into a discharge period.

D. Convective Heating and Large-Scale Circulations

The results of the previous two sections show that the generation of the MJO entails a gradual deepening of moisture with instability during the recharge period, and a very moist column for periods of intense convection during the transition to the discharge period. But how does this moist column affect the generation of the MJO? A possible answer is through the intense heating generated by convection occurring in a very moist environment.

This study examines heating in the context offered up by Yanai et. al. (1973), who used

$$Q_1 \equiv Q_R + L(c - e) - \frac{\partial}{\partial p} \overline{s' \omega'} = c_p \left[\frac{\partial T}{\partial t} + \mathbf{v}_h \cdot \nabla_h T + \left(\frac{p}{p_o} \right)^\kappa \omega \frac{\partial \theta}{\partial p} \right]$$

$$Q_2 \equiv L(c - e) + L \frac{\partial}{\partial p} \overline{q' \omega'} = -L \left[\frac{\partial q}{\partial t} + \mathbf{v}_h \cdot \nabla_h q + \omega \frac{\partial q}{\partial p} \right]$$

the terms Q_1 and Q_2 to describe the apparent heat source and the apparent moisture sink defined by the equations:

Based on these definitions, Q_1 is the heating due to radiative heating, latent heating, and small-scale vertical transport of dry static energy in the column. Q_2 is then drying which is the sum of the difference between evaporation and precipitation, and small-scale vertical transport of water vapor. These processes are all simulated using parameterizations (or super-parameterizations) in the CAM and SP-CAM, so my plots of these variables come from two sources. The Q_1 plots are created using a variable that includes “all temperature tendencies due to physics” and the Q_2 plots use a variable described as including “all water-vapor tendencies due to physics.”

As can be seen in Figures 31 and 32, the relationships between precipitation and heating the troposphere are very different between the two models. In Figure 31, total magnitude of

Q_1 heating during heavy rain events in the SP-CAM is quite different from the traditional CAM. Where the SP-CAM sees heating rates maximize at above 70 K day^{-1} , the CAM only sees heating up to at 40 K day^{-1} . This is largely because the CAM does not produce rain events as intense as those of the SP-CAM, and for a given rainrate in the composite, the maximum values of heating in the column are actually similar. We have shown previously that the number of clear, dry days in the MFR is important for the recharge period, but the intensity of rain during the discharge period is also important. The CAM is unable to generate the magnitudes of heating seen in the SP-CAM because it cannot produce the magnitudes of rainrates either.

The SP-CAM also sees heating through a large portion of the column, where the heating in the traditional CAM is squeezed, or much lower in general, at and below about 700 hPa, as seen in many variables previously. The Q_1 variable includes the radiative effects of clouds, the latent heating effects, and the vertical transports. The deeper region of Q_1 heating in the SP-CAM is probably a result of more latent heating through the column and lowered ARC (Figure 20). These properties are both increased by moisture in the column. A more moist environment increases the precipitation efficiency, or rate at

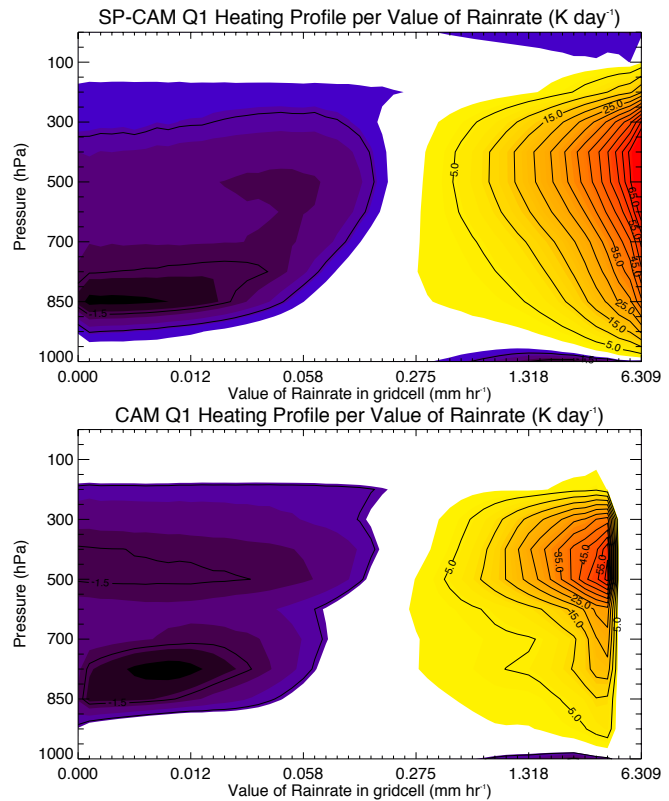


Fig 31: Q_1 heating rate (apparent heating source) profiles per value of rainrate in the SP-CAM (top) and the CAM (bottom). Both of these values are calculated from the total temperature tendency due to all physics parameterizations in both models

which vapor is condensed and removed from the atmosphere through precipitation as a function of the amount of available water vapor. Increased water vapor in an environment where precipitation is forming reduces the amount of re-evaporation of rain drop water, and vapor is more quickly and efficiently converted to large precipitation water droplets. This more efficient condensation of vapor produces more liquid water and more latent heating. A more humid column also traps upwelling longwave radiation better than dry air, and so reduces the ARC. These two effects alone are enough to greatly increase the heating due to convection through the column in the SP-CAM as seen in Figure 31.

Another important difference in the two plots includes the depth and intensity of Q_1 cooling over lower rainrates. In the CAM, this is caused by the very low amounts of water vapor in those layers (see Figure 24), which allows the atmosphere to cool radiatively much

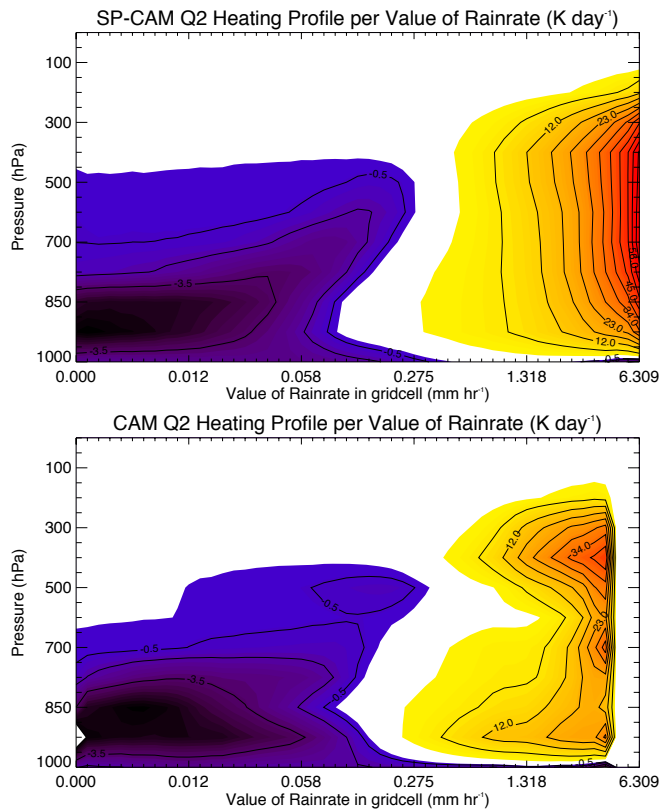


Fig 32: Q_2 drying rate (apparent moisture sink) profiles per value of rainrate in the SP-CAM (top) and the CAM (bottom). These values are calculated from the total water vapor tendency due to all physics parameterizations in both models.

more intensely than same layers of the SP-CAM (Figure 20), which have a higher relative humidity in the composite.

The Q_2 heating in Figure 32 is even more telling. Again, the total maximum value of heating above heavy rain events in the SP-CAM (above 40 K day^{-1}) is much higher than that above heavy rain events in the CAM (only 28 K day^{-1}). This larger, more intense Q_2 can also be explained by the increased amount of moisture in the column above

heavy rain events in the SP-CAM. Similar to the arguments for the increased Q_1 , the precipitation efficiency, and therefore condensation, increases with increased moisture in the region. Also, the higher vertical velocities shown over heavy rainrates in Figure 17 will increase the apparent sink of moisture in the columns of the SP-CAM through a more rapid convective lifting and drying process.

Again, the heating in the SP-CAM fills the entire column, while the heating in the CAM is pinched between 850 and 600 hPa. However, unlike Figure 31, the Q_2 heating, or the apparent moisture sink, is larger around 850 hPa in the lower panel of Figure 32. This coincides with an increase in the relative humidity at these levels in the CAM as shown in Figure 24 as well. Finally, the Q_2 cooling, or the apparent vapor source, for lower rainrates is much more intense in the CAM than the SP-CAM. This is likely due to the fact that the heavily stable layer above lower rainrates (see Figure 18) prevents convective lifting of vapor above the lowest levels. This paints the image of heavily subsiding dry air above low clouds in low precipitation regimes. This extremely dry air will also evaporate any cloud transport of vapor that might make it through the inversion, which adds to the Q_2 cooling. Also, in the SP-CAM, there is an obvious tongue of cooling reaching upwards from 850 to 500 hPa. This is an increase of water vapor that begins at low levels, gradually increases in height, and is a result of medium-intensity convective processes. The CAM does not produce this strong signal, indicating once more that convection is not as capable of moistening the layers between 850 and 500 hPa in this model.

Column heating and moisture differences are significant, and impact the formation of the MJO in the two models. The plots of composite wave passages in Figures 33 and 34 show the importance of convective heating for the MJO in the models and the real world. In the SP-CAM, as the MJO approaches, the heating due to convection intensifies, spreads through the column, and then remains at a high level for several days during the period of

average peak rainfall, and average minimum non-filtered OLR, or during the discharge period. While the convection is heating and drying these upper layers so powerfully, a cooling and moistening trend in Q_2 appears below. After the peak rainfall, the cooling and moistening intensifies and spreads vertically through several layers of the mid-troposphere. Similar patterns can be seen in the TOGA-COARE plots. Both Q_1 and Q_2 strengthen and move into the upper levels of the troposphere as the peak rain-rates approach. Around the period of the most intense rainfall, a strong moistening signal appears in the lower levels of the Q_2 profile and spreads vertically while it intensifies after the passage of the intense convection. The CAM, however, does not follow this specific pattern. In general, weaker heating occurs in the upper levels (between 500 and 200 hPa) for almost the entire period. The heating does occasionally approach the intensity of the heating seen in the SP-CAM plots, but it does not persist for long. And throughout the entire period, there is generally only weak heating or strong cooling at middle levels (between 850 and 500 hPa).

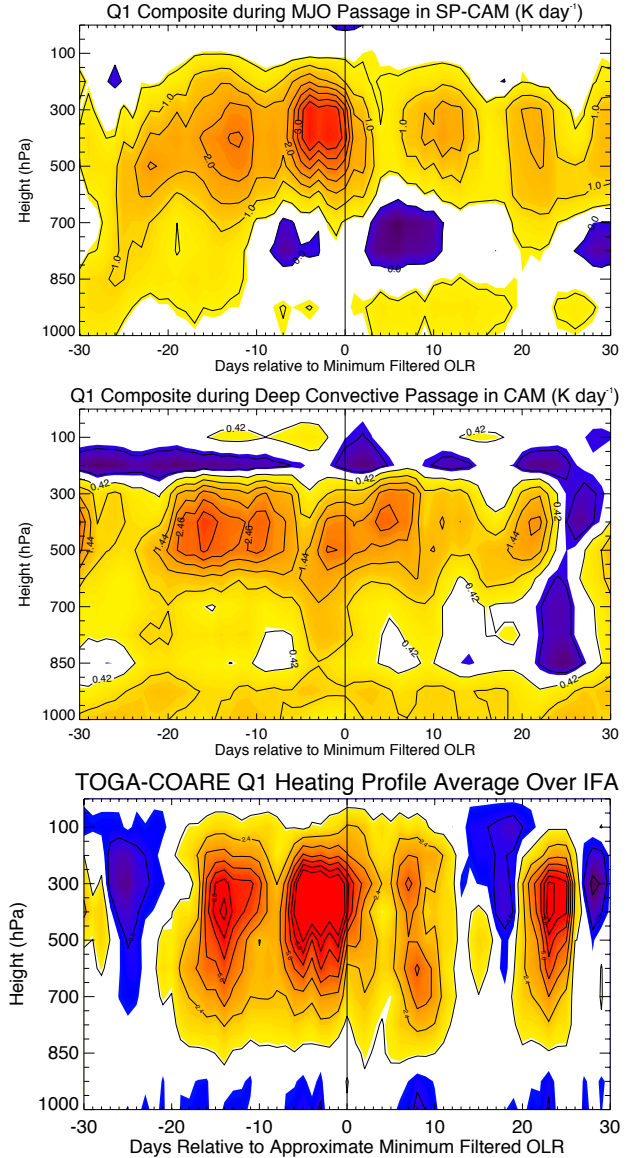


Fig 33: Profile of Q_1 with the passage of a composite MJO event in the SP-CAM (top), CAM (middle) and the IFA-average derived Q_1 smoothed with a 5 day running mean for the first MJO event during TOGA-COARE (bottom).

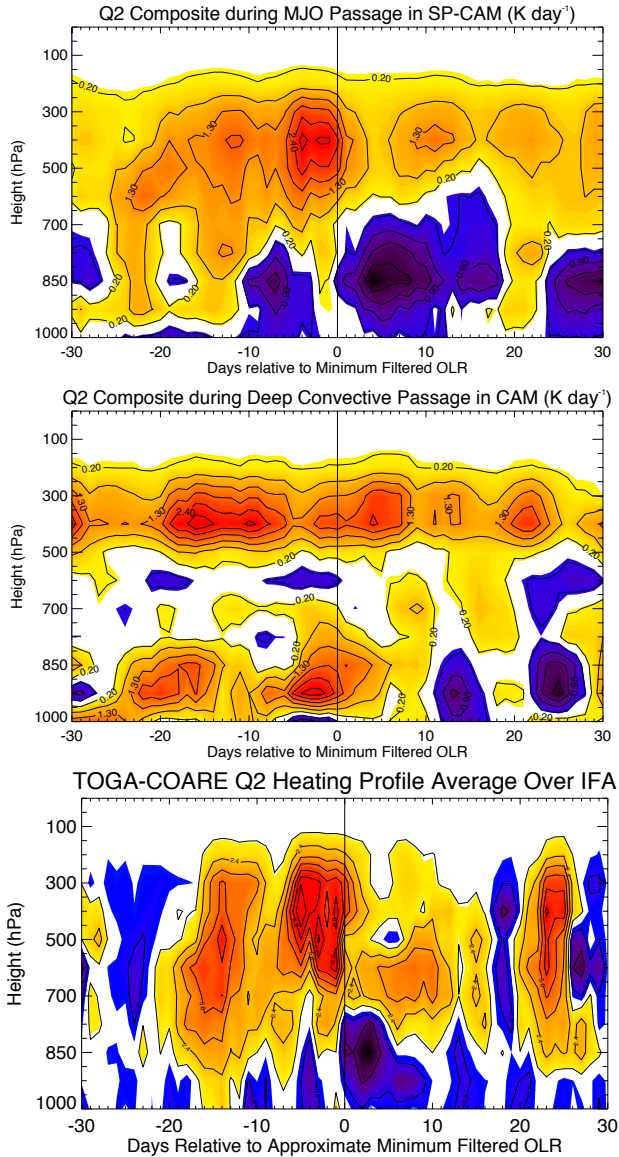


Fig 34: Profile of Q_2 with the passage of a composite MJO event in the SP-CAM (top), CAM (middle) and the IFA-average derived Q_2 smoothed with a 5 day running mean for the first MJO event during TOGA-COARE (bottom).

The strong convective heating is important during the discharge period. We have previously shown that this is a time of intense precipitation in a nearly saturated column. When convection occurs in these conditions, local downdrafts are also very moist, and small scale convective circulations are not as effective at reducing instability. This allows convection to run a little longer, and a little “hotter”, producing more intense heating.

As predicted by the models of Gill (1980) and Matsuno (1966), this heat source forces a large-scale surrounding circulation. Large scale circulation patterns work to transport heat out of the region at upper levels and advect in cooler, dryer air from the midlatitudes at lower levels. The large scale wind

and relative humidity patterns can be seen in Figure 35. Strong southwesterly winds created at the intersection of two Rossby gyres in the SP-CAM move dryer air in below the intense convection at this point (the map is centered at the location of minimum filtered OLR). The CAM, however, does not appear to produce this surrounding large scale structure in Figure 35 or other events not shown here. This is because convection is not occurring in a

nearly-saturated column, and it is not producing the intense heating required to spawn surrounding circulation patterns.

Put together, the SP-CAM and the observations begin to tell a story about the interactions of convection and heating with large-scale waves in the tropical warm pool. It begins with shallow convection during the most common state of the tropical warm pool: warm sunny skies and light easterly winds. Large-scale subsidence and slightly drier air

dominate in the atmosphere above the shallow trade-wind cumuli. As lower levels mix and moisten, small scale convective events pop up, and begin to moisten slightly higher and higher areas of the tropical troposphere. Localized circulations pass quickly, as their downdrafts cool below and precipitation bleeds the excess moisture from the cloud. However, with each passage, the tropical atmosphere becomes more moist and local downdrafts are less effective at cooling the boundary layer and re-stabilizing the local environment.

Eventually, the warm tropical air becomes thick enough with moisture that deep convection fills the column, and forms a large, powerful, heating source. If the heating is strong enough, and persists for a long enough period of time, a larger scale circulation forms to help restore the system to stability. Rossby gyres form to the north and south of this violent convective system, and a Kelvin wave forms to the east. The Rossby gyres work together to

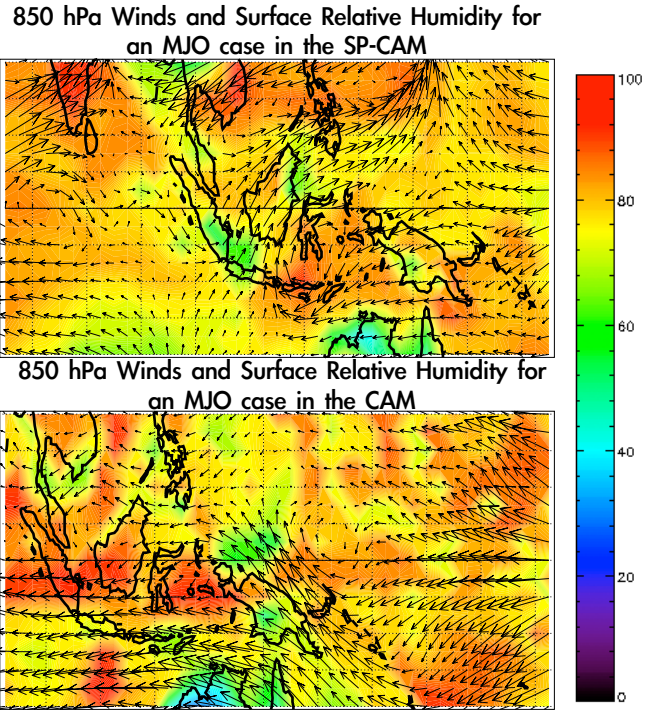


FIG 35: Surface wind speed (vectors) and surface relative humidity (color contours) for an MJO or strong rain event at minimum filtered OLR in the SP-CAM (top) and the CAM (bottom). Maximum vector for SP-CAM is magnitude 22m/s and maximum vector for CAM is magnitude 16m/s.

form a westerly wind burst on the western side of the convection. They advect in dry air from the sub tropics, which finally help to cool the lower layers (through precipitation evaporation, and cool air advection). This helps stabilize the western side of the convection, but the Kelvin wave aids in convergence of moist destabilized air on the eastern side. More deep convection forms to the east while older systems die out on the west, and the broad envelope of convection and convective heating moves slowly eastward, which drags the large scale circulation along with it. As this MJO propagates through the warm pool, it rains out moisture from overly-saturated and destabilized air, leaving a dryer, more stable, tropical atmosphere with suppressed convection in its wake, and the entire region returns to a stable and suppressed state. The cycle begins again, and the time required to re-moisten and destabilize the region results in the periodicity of the MJO. After the passage of each disturbance, the re-stabilized air and suppressed convective regime reigns, for the time being. It will only be a few short weeks before the tropics are again destabilized to their tipping point, and the deep convective envelope of the MJO appears once more.

Chapter 4: Summary and Future Work

Our atmosphere can do amazing things. Our study has demonstrated the amazing power, adaptability and importance of tropical convection from a variety of perspectives. But one important theme runs through the entire discussion. We have shown in this study, in many different ways and in sharp detail, the importance of the complex interactions of convection and water vapor to the appearance and intensity of the MJO.

We began with a view from high above, showing that the MJO is, at its most basic, a huge region of convection that appears in the Indian Ocean every 30 to 70 days, and slowly travels eastward towards the maritime continent and western Pacific. We also saw that GCMs have had trouble representing the most elemental properties of this globally significant disturbance for many years. Lin et al. (2006) enumerated the many modern climate models that, despite years of work and research, were still unable to accurately represent intraseasonal oscillations. Their study implicated the statistical representations of the convection, or convection parameterizations, in each model as the most likely source of inaccuracies leading to poor representation of the MJO. In order to learn more about the tropical oscillation and the problems within GCMs, we introduced our two main data sources: four year global atmospheric simulations from the traditional CAM and SP-CAM, which implement different convection parameterizations, and result in the transformation of the MJO in the CAM from basically non-existent to extremely intense and vigorous in the SP-CAM.

We then zoomed in closer and examined the observed structure and life-cycle of the MJO. Madden and Julian (1971, 1972) described a large region of convection which forms in the central regions of the Indian Ocean and travels slowly eastward across the maritime

continent to about 180 degrees longitude, where the convection dies out and dry, quick moving wind anomalies can continue to propagate from there. The convection is not a simple storm, but has been shown to be more of a convective envelope containing many different scales of convective disturbances, which travel west as the envelope propagates to the east. Other studies have determined that the convective envelope exists in a complex large-scale vertical structure, with convergence at the surface, divergence aloft, a Kelvin wave east of the center and a pair of Rossby gyres producing strong westerly winds to the west of the center. Surrounding the region of powerful convection are large swaths of ocean beneath sinking air with suppressed convection. The question of the initiation source and cause of the periodic reappearance of the system led us into a discussion of the Discharge-Recharge oscillation (DRO) proposed by Bladé and Hartmann (1993).

The DRO produces an MJO on a regular timescale dictated by the amount of time required for the tropical regions to moisten and destabilize in a suppressed convection regime. After 30 to 70 days of increasing moisture and instability, the tropical Indian Ocean reaches a “tipping point” and large scale convection can be triggered simply through a random interaction of the extra tropics with the unstable tropical atmosphere. The convection works to discharge the pent up energy in the region as it slowly propagates to the east. After this discharge, the tropical regions exist in a dryer regime, with deep convection suppressed by the sinking branches of the MJO circulation, and the recharge period begins again.

After this detailed view of the structure, processes and mechanisms involved in the MJO, we turned our focus towards the representation of these processes in our two models, the CAM and SP-CAM. The CAM contains four different parameterizations to represent the sub-grid scale processes associated with clouds and convection. These parameterizations involve many assumptions and simplifications, which are outlined in Table 1. The most pertinent to our discussion is the fact that the deep convection parameterization (Zhang and

McFarlane, 1995) does not allow detrainment below the mid-tropospheric minimum in saturation moist static energy, due to an arbitrary constraint. This scheme produces the majority of the heavy rainfall in the model, but does not adequately moisten through the column. The shallow convection parameterization (Hack, 1994) does a better job of mixing moisture from lower layers into the middle troposphere, but it is not particularly active during periods of intense rainfall (see Figure 23). This results in a significant disconnect between the effects of convection on moisture and precipitation in the column. The SP-CAM does not use traditional convection parameterizations, but instead has a two dimensional CRM embedded within each GCM gridcell. There are still assumptions and simplifications related to convection in this version of the SP-CAM, but clouds, rain, and the transportation of moisture through the column are all explicitly simulated, and the various aspects of sub-grid scale convective circulations, including moisture sources, sinks and transportation, are all directly coupled through the CRM.

The view of convective processes within the models produced by this discussion led us to begin composition of a panoramic illustration of tropical atmospheric processes involved in the creation and maintenance of an MJO. We started with a look at the large scale properties of the MFR. Here we saw that the CAM has trouble reproducing realistic surface zonal winds (Figure 15) as well as the observed distribution of rainrates (Figure 16). Analysis of vertical motion (Figure 17), static stability (Figure 18), profiles of potential temperature (Figure 19), and moist static energy (Figure 21) as functions of precipitation rate revealed a reoccurring pattern in the CAM. The disconnection between the formation of heavy precipitation by the deep convective parameterization and the moistening provided by the shallow convective scheme results in an unrealistically dry middle and lower troposphere in the model.

In lighter rain regimes, the dryness of the mid troposphere causes a higher atmospheric radiative cooling rate (Figure 20), resulting in stronger subsidence and a higher static stability. These issues can create a stronger-than-observed inhibition of convection during dryer regimes, and prevent penetrating convection that would help to increase moisture through the column. When convection does penetrate to the upper levels, and the gridcell moves into a heavy rain regime, the deep convection parameterization prevents detrainment of moisture below the minimum of saturation moist static energy, which occurs around 700 hPa (Figure 21). This results in vertical discontinuities around and just above 700 hPa for a variety of variables, including vertical velocity, temperature and relative humidity. The SP-CAM, on the other hand, has a weaker minimum of moist static energy, indicating that much of the column is very well mixed during heavy convective events. Profiles of static stability and potential temperature are much more vertically continuous in this model, even slightly more-so than the ERA-40 data used as an observational proxy. The SP-CAM also has weaker subsidence and static stability over light rain regions, which would allow convection to more easily penetrate and moisten through many levels.

The next element of the panorama was an exploration of convective-scale moistening and drying processes. Here we can see clearly how dry the CAM is compared to the SP-CAM and observations. The total column water vapor is dryer for almost all values of rainrates (Figure 22) and the dry region above light rainrates and below 700 hPa for heavy rainrates is especially obvious (Figure 24). The SP-CAM, however, seems overly moist, with a high TPW and very moist column for all rainrates above about 1 mm hr^{-1} . An investigation of the moisture budgets shows that, in the short term, precipitation in the CAM very quickly removes vapor from the column (Figure 25). The CAM also has very high wind values for these high rainrates (Figure 27) which cause higher evaporation during these intense rain events and counter the rapid drying by precipitation on the longer timescale (Figure 26).

The SP-CAM produces a wider range of variation with rainrate, with low rainrates drying, middle intensity rain adding moisture, and only the most intense rain drying (Figure 25). The drying as a function of rainrate would likely increase if this model did not also have high winds during heavy precipitation events (Figure 27), resulting in higher evaporation values to counter the drying via precipitation (Figure 26). This is very similar to the convection-wind-evaporation feedback described by Luo and Stephens (2006). The high winds in the SP-CAM may be caused by the lack of momentum feedback from the CRM to the GCM, so the large-scale wind field does not feel the drag produced by the deep convection. The surface parameterizations are unaffected by the CRM in the SP-CAM, so the evaporation parameterization remains the same, and works to continually pump moisture into the columns with heavy rainrates and high winds. This explains the over-moistening and the weak short-term drying in the column due to intense rainrates.

After examining both the large-scale properties and convective processes of the MFR in the models and observations, the next step is to take a look at how these affect the MJO and the DRO. Our analysis showed a build up of moisture through the column (Figure 28), increasing rainrates and TPW, and decreasing OLR (Figure 30) as the disturbance approached in the SP-CAM, but the CAM remained dry as heavy rain events occurred, and the increases in rainrate and TPW were very poorly correlated during these events. We then show the inevitable disruption in the DRO in the CAM, as compared to the SP-CAM and observations (Figure 29). The SP-CAM and observations show a more correlated pattern during the course of the DRO, with rainrates and TPW increasing together during the recharge period and decreasing together during the discharge period. Due to the unrealistic relationships between moistening and precipitation in the CAM, the DRO is less systematic and more of a wandering path. In the recharge period as simulated by the CAM, rainrates first increase with little increase in TPW, then TPW increases after rainrates have already peaked and

begun to decrease. This prevents the CAM from priming the environment for deep convection during the recharge period, and prevents a transition into a powerful discharge period. The cycle is broken, and no realistic MJO appears in the CAM.

Finally, we examined why these complex interactions of convection and water vapor are so critical to the appearance and intensity of the MJO by looking at Q_1 , the apparent convective heat source and Q_2 , the apparent moisture sink. The final piece of the picture is shown through the profiles of these heating terms as the MJO builds and passes. In the observations and the SP-CAM, heating grows from the surface to the upper levels during the recharge period. An intense heating occurs in the upper atmosphere, and lingers for a few days during the discharge period. A moistening and cooling begins to appear beneath this heating during the discharge period, and slowly spreads upwards, shutting off the heavy convection and returning the region to a stable and suppressed state (Figures 33 and 34). These patterns of heating and convective drying before the event and cooling and convective moistening afterwards are simply not apparent in the CAM. Without the strong lingering heat source due to convection, the surrounding large-scale circulation cannot form in the CAM, and the MJO is not present.

When we step back to see the entire view, the story is clear. The connections between moisture and convection are extremely important to the MJO for a variety of reasons. Short lived, penetrating convection primes the atmosphere for deep convection during the recharge period of the oscillation through transport and evaporation of moisture at all levels. Once the atmosphere is very moist, convection is less able to dry and re-stabilize through local processes. This is the point where the strongest heating forms and remains for a few days, until the surrounding circulations appear during the discharge period, and help to re-stabilize the region through the advection of dry subtropical air and large-scale transport of heat and energy throughout the tropics.

Our view begins and ends with the same themes. The appearance of the MJO is based on the time period required to moisten and destabilize the troposphere above the Indian Ocean and western Pacific. The CAM is unable to produce a moistened atmosphere through many levels, because of unrealistic constraints placed on its convection parameterizations. Without a nearly saturated column, convection soon dissipates as it rapidly re-stabilizes the local atmosphere. The SP-CAM produces an overly moist column due to unrealistic winds and evaporation during convective events. In the real tropics and the SP-CAM, the convection within a high-humidity environment produces a more intense heating and spawns the large-scale circulation that is the signature of the MJO. In the end, the appearance of the MJO is based on water vapor build up from sub-grid scale processes that are difficult to simulate in a traditional model. The release of energy by the large scale circulation can be resolved on a GCM scale, but that does not matter if the heating required to produce the circulation does not persist long enough or never appears in the first place.

The final point we must focus on is future work. There are still so many questions to be answered. What exactly causes the scale selection, or longitudinal size, of the disturbance? What causes it to change speeds of propagation during its lifecycle? How does the MJO interact with the ocean's surface or the El Nino/Southern Oscillation (ENSO)? How does the MJO interact with Asian monsoon, the Indian Ocean dipole (IOD), and extra tropical circulations? Being able to predict the onset of MJO convection and impacts of the disturbance around the planet could improve forecasting skill by huge amounts (Donald et al. 2006). Thankfully, there are plenty of new and interesting tools available to help answer these questions and many more. There are new versions of GCMs which include other super parameterizations (Chern et al. 2006) or are global domain cloud resolving models (Iga et al. 2004). Even the CAM has recently released a new version (3.5 personal communications with Richard Neale at NCAR) and a version 4.0 is currently being worked on (personal

communications with Richard Neale at NCAR). There are also many new and very useful observational tools for the tropical regions of the planet. CloudSat and the A-train satellites provide an unprecedented view of the vertical structure of the atmosphere (Stephens et al. 2002), which could give valuable insight into the structure of clouds in the MJO. There have been several more observational field experiments in the region over the last few years and there are plans for many more (Waliser 2007). The many questions posed about the MJO are important, and the future looks very bright for finding the answers.

References

- Arakawa, A., A. Katayama, and Y. Mintz, 1968: Numerical simulation of the general circulation of the atmosphere. *Proceedings of the WMO/IUGG Symposium on Numerical Weather Prediction, Tokyo*. pp. IV-7 to IV-8-12.
- Benedict, J. J. and D. A. Randall, 2007: Observed Characteristics of the MJO Relative to Maximum Rainfall. *J. Atmos. Sci.*, in press.
- Blade, I. and D. L. Hartman, 1993: Tropical Intraseasonal Oscillations in a Simple Nonlinear Model. *J. Atmos. Sci.*, **50**, 2922-2939.
- Bonan, G. B., 1997: Effects of Land Use on the Climate of the United States. *Climatic Change*, **37**, 449-486.
- Bony, S. and K. A. Emanuel, 2005: On the Role of Moist Processes in Tropical Intraseasonal Variability: Cloud-Radiation and Moisture-Convection Feedbacks. *J. Atmos. Sci.*, **62**, 2770-2789.
- Bony, S., K.-M. Lau, and Y. Sud, 1997: Sea surface temperature and large-scale circulation influences on tropical greenhouse effect and cloud radiative forcing. *J. Climate*, **10**, 2055-2077.
- Chern, J and W. Tao, X. Lin, 2006: Application of the Goddard Multi-scale Modeling Framework in Climate Simulation. *EOS Trans. AGU*, 87(36), Jt. Assem. Suppl., Abstract A53B-02.
- Ciesielski, P.E., L.M. Hartten, and R.H. Johnson, 1997: Impacts of merging profiler and rawinsonde winds on Toga COARE analyses. *J. of Atmos. Oceanic Tech.*, **14**, 1264-1279.

- Collins, W. D. and Coauthors, 2004: Description of the NCAR Community Atmosphere Model (CAM 3.0). *NCAR Technical Note*.
- Covey, C., S. H. Schneider, and S. L. Thompson, 1984: Global atmospheric effects of massive smoke injections from a nuclear war: results from general circulation model simulations. *Nature*, **308**, 21-25.
- Donald, A. and coauthors, 2006: Near-global impact of the Madden-Julian Oscillation on rainfall. *Geo. Res. Let.*, **33**, L09704, doi:10.1029/2005GL025155.
- Gates, W. L., 1992: AMIP: The Atmospheric Model Intercomparison Project. *Bul. Amer. Met. Soc.*, **73**, 1962-1970.
- Gneiting, T. and A. E. Raftery, 2005: Weather Forecasting with Ensemble Methods. *Science*, **310**, 248-249.
- Hack, J. J., 1994: Parameterization of moist convection in the National Center for Atmospheric Research Community Climate Model (CCM2). *J. Geophys. Res.*, **99**, 5551-5568.
- Hu, Q., and D. A. Randall, 1994: Low-frequency oscillations in radiative-convective systems. *J. Atmos. Sci.*, **51**, 1089-1099.
- Iga, S. and H. Tomita, M. Satoh, T. Nasuno, and K. Goto, 2004: A Global Cloud Resolving Model NICAM (Nonhydrostatic ICoshedral Atmospheric Model) on the Earth Simulator. *EOS Trans. AGU*, West. Pac. Geophys. Meet. Suppl., Abstract U23A-02.
- Inness, P. M., and J. M. Slingo, E. Guilyardi, and J. Cole, 2003: Simulation of the Madden-Julian oscillation in a coupled general circulation model. Part II: The role of the basic state. *J. Climate*, **16**, 365-382.
- Jakob, C., G. Tselioudis and T. Hume, 2005: The Radiative, Cloud, and Thermodynamic Properties of the Major Tropical Western Pacific Cloud Regimes. *J. Climate*, **18**, 1203-1215.

- Kemball-Cook, S. R., and B. C. Weare, 1996: The onset of convection in the Madden-Julian oscillation. *J. Climate*, **14**, 780-793.
- Khairoutdinov, M. F. and D. A. Randall, 2001: A cloud resolving model as a cloud parameterization in the NCAR Community Climate System Model: Preliminary results. *Geophys. Res. Lett.*, **28**, 3617-3620.
- Khairoutdinov, M. F., and D. A. Randall, 2003: Cloud resolving modeling of the ARM Summer 19 97 IOP: Model formulation, results, uncertainties, and sensitivities. *J. Atmos. Sci.*, **60**, 607– 625.
- Khairoutdinov, M. F., D. A. Randall, and C. DeMott, 2005: Simulations of the atmospheric general circulation using a cloud-resolving model as a super-parameterization of physical processes. *J. Atmos. Sci.*, **62**, 2136–2154.
- Kummerow, C., and Coauthors, 2000: The Status of the Tropical Rainfall Measuring Mission (TRMM) after Two Years in Orbit. *J. Appl. Meteor.*, **39**, 1965-1982.
- Lau, K.-M., L. Peng, C.-H. Sui, and T. Nakazawa, 1989: Dynamics of super cloud clusters, westerly wind bursts, 30-60 day oscillations and ENSO: an unified view. *J. Meteorol. Soc. Jpn.*, **67**, 205-219.
- Lin, J. and Coauthors, 2006: Tropical Intraseasonal Variability in 14 IPCC AR4 Climate Models. Part I: Convective Signals. *J. Climate*, **19**, 2665-2690.
- Luo, Z. and G. L. Stephens, 2006: An enhanced convection-wind-evaporation feedback in a superparameterization GCM (SP-GCM) depiction of the Asian summer monsoon. *Geo. Res. Lett.*, **33**, L06707, doi:10.1029/2005GL025060
- Madden, R. A., and P. R. Julian, 1971: Detection of a 40-50 Day Oscillation in the Zonal Wind in the Tropical Pacific. *J. Atmos. Sci.*, **28**, 702-708.
- Madden, R. A., and P. R. Julian, 1972: Description of Global-Scale Circulation Cells in the Tropics with a 40-50 Day Period. *J. Atmos. Sci.*, **29**, 1109-1123.

- Madden, R. A., and P. R. Julian, 1994: Observations of the 40-50-Day Tropical Oscillation - A Review. *Mon. Wea. Rev.*, **122**, 814-837.
- Maloney, E. D., and D. L. Hartmann, 2001a: The Madden-Julian oscillation, barotropic dynamics, and North Pacific tropical cyclone formation. Part I: Observations. *J. Atmos. Sci.*, **58**, 2545-2558.
- Manabe, S. J. Smagorinsky, and R. F. Strickler, 1965: Simulated climatology of a general circulation model with a hydrological cycle. *Mon. Wea. Rev.*, **93**, 769-798.
- Manabe, S., K. Bryan, and M. J. Spelman, 1979: A global ocean-atmosphere climate model with seasonal variation for future studies of climate sensitivity. *Dyn. Atmos.-Oceans*, **3**, 393-426.
- McFarlane, S. A., J. H. Mather, and T. P. Ackerman, 2007: Analysis of tropical radiative heating profiles: A comparison of models and observations. *J. Geophys. Res.*, **112**, D14218, doi: 10.1029/2006JD008290.
- Miller, A. J., S. Zhou, and S.-K. Yang, 2003: Relationship of the Arctic and Antarctic Oscillation to outgoing longwave radiation. *J. Climate*, **16**, 1583-1592.
- Nakazawa, T., 1988: Tropical super clusters within intraseasonal variations over the western Pacific. *J. Meteor. Soc. Japan*, **64**, 17-34.
- Rasch, P.J., M. C. Barth, J. T. Kiehl, S. E. Schwartz, and C. M. Benkowitz, 2000: A description of the global sulfur cycle and its controlling processes in the National Center for Atmospheric Research Community Climate Model, Version 3. *J. Geophys. Res.*, **105**, 1367-1385.
- Rui, H., and B. Wang, 1990: Development characteristics and dynamic structure of tropical intraseasonal convection anomalies, *J. Atmos. Sci.*, **47**, 357-379.
- Slingo, J. M. and Coauthors, 1996: Intraseasonal oscillations in 15 atmospheric general circulation models: Results from an AMIP diagnostic subproject. *Climate Dyn.*, **25**, 117-140.

- Solomon, S., D. and Coauthors, 2007: Technical Summary. In: *Climate Change 2007: The Physical Science Basis. Contribution of Working Group I to the Fourth Assessment Report of the Intergovernmental Panel on Climate Change*. Cambridge University Press, Cambridge, United Kingdom and New York, NY, USA.
- Stephens, G. L., and Coauthors, 2004: Observational Evidence for the Mutual Regulation of the Tropical Hydrological Cycle and Tropical Sea Surface Temperatures. *J. Climate*, **17**, 2213-2224.
- Stephens, G. L., and D. G. Vane, R. J. Boain, G. G. Mace, K. Sassen, Z. Wang, A. J. Illingworth, E. J. O’Conner, W. G. Rossow, S. L. Durden, S. D. Miller, T. R. Austin, A. Benedetti, C. Mitrescu, 2002: The CloudSat mission and the A-Train. *Bull. Amer. Meteorol. Soc.*, **83**, 1771-1790.
- Sundqvist, H., 1988: Parameterization of condensation and associated clouds in models for weather prediction and general circulation simulation. In: *Physically-based Modeling and Simulation of Climate and Climate Change*, Vol. 1, edited by M. E. Schlesinger, 433-461, Kluwer Academic.
- Uppala, S.M., and Coauthors, 2005: The ERA-40 re-analysis. *Quart. J. R. Meteorol. Soc.*, **131**, 2961-3012. doi:10.1256/qj.04.176
- Waliser, D., 2007: Year of Tropical Convection. *US. CLIVAR MJO Wkshp*, Irvine CA.
- Wang, W. and M. E. Schlesinger, 1999: The Dependence on Convection Parameterization of the Tropical Intraseasonal Oscillation Simulated by the UIUC 11-Layer Atmospheric GCM. *J. of Climate*, **12**, 1423-1457.
- Webster, P.J., and R. Lukas, 1992: TOGA COARE: The Coupled Ocean- Atmosphere Response Experiment. *Bull. Am. Meteorol. Soc.*, **73**, 1377-1416.

- Wheeler, M. and G. N. Kiladis, 2003: Convectively Coupled Equatorial Waves: Analysis of Clouds and Temperature in the Wavenumber-Frequency Domain. *J. Atmos. Sci.*, **56**, 374-399.
- Yanai, M., S. Esbensen, and J.-H. Chu, 1973: Determination of bulk properties of tropical cloud clusters from large-scale heat and moisture budgets. *J. Atmos. Sci.*, **30**, 611-627.
- Yanai, M., B. Chen, and W.-W. Tung, 2000: The Madden-Julian Oscillation Observed during the TOGA COARE IOP: Global View. *J. Atmos. Sci.*, **57**, 2374-2396.
- Zhang, C., 2005: Madden-Julian Oscillation. *Rev. Geophys.*, **43**, RG2003, doi:10.1029/2004RG000158.
- Zhang, G. J. and N. A. McFarlane, 1995: Sensitivity of climate simulations to the parameterization of cumulus convection in the CCC-GCM. *Atmos.-Ocean*, **3**, 407-446.